CHAPTER FOUR

Light Modes of Free Space

Uri Levy, Stanislav Derevyanko, Yaron Silberberg
Weizmann Institute of Science, Rehovot, Israel

Contents

1. INTRODUCTION

Free space propagation of both paraxial and nonparaxial optical beams has attracted steady attention of researchers over the last four decades. For time-harmonic beams, the main physical effect describing their change of shape during the propagation is linear diffraction (Goodman, 1988; Yariv & Yeh, 1984). For a generic optical beam, the free space diffraction leads to broadening of the pattern in the transverse direction as different spatial harmonics of the beam propagate at different angles with the optical axis.

Progress in Optics, Volume 61
ISSN 0079-6638
http://dx.doi.org/10.1016/bs.po.2015.10.001

However, since the late 80s an interesting class of nondiffracting beams was introduced (Durnin, 1987; Durnin, Miceli, & Eberly, 1987). This introduction has spurred the interest not only in the diffraction of paraxial beams but also in the generic class of the free space solutions of Maxwell's (or rather 3D Helmholtz) equations commonly known as *propagation invariant optical fields* (*PIOFs;* see, for example Bandres, Gutiérrez-Vega, & Chávez-Cerda, 2004; Gutiérrez-Vega & Bandres, 2005; Gutiérrez-Vega, Iturbe-Castillo, & Chávez-Cerda, 2000; Siviloglou & Christodoulides, 2007).

PIOFs received special attention in a comprehensive review by Turunen and Friberg (2009), including discussion of custom designs, vectorial extension, and partial coherence.

Over the years, many distinct light patterns solving the exact and the approximated homogeneous wave equation were presented and studied by different research groups. With the growing number of introduced free space light patterns, there is a pressing need to collect and classify these patterns in an organized manner according to their key optical properties, and to present characteristic distribution maps.

The current short review serves exactly this purpose and can be viewed as the first step toward such a classification. It represents a compendium and tentative classification of currently known light patterns, or light modes—the solution sets of free space Maxwell's equations. We begin by first dividing the light pattern sets discussed in this review into two major groups: Waves and Beams. Waves (sometimes termed PIOFs as mentioned above), are the sets solving Helmholtz equation (HE); and Beams, are the sets solving the paraxial wave equation. Next, we divide Waves and Beams into subgroups, according to the coordinate system to which they belong. For each subgroup, we concisely list their main physical and mathematical properties.

1.1 Waves

For fully self-contained treatment of the problem, we shall start with a standard derivation of the electromagnetic wave equation (Yariv & Yeh, 1984). Assuming a **monochromatic** (time-harmonic) electromagnetic wave of frequency ω, Maxwell's equations for the electrical field $[\boldsymbol{E}(\boldsymbol{r})]$, in the absence of free currents and free charges, can be arranged as:

$$\nabla^2 \boldsymbol{E}(\boldsymbol{r}) + k_0^2 \cdot \epsilon(\boldsymbol{r}) \cdot \boldsymbol{E}(\boldsymbol{r}) = -\boldsymbol{\nabla}[\boldsymbol{\nabla} \circ \boldsymbol{E}(\boldsymbol{r})] \tag{1}$$

where k_0 is the vacuum wave-vector ($=\omega/c$) and $\epsilon(x,y,z)$ is the medium permittivity.

Given a homogeneous-permittivity medium (free space):

$$\epsilon(x,y,z)\equiv\epsilon_H \Longrightarrow -\nabla[\nabla\circ\boldsymbol{E}(\boldsymbol{r})]=0, \tag{2}$$

Equation (1) is reduced to the scalar wave equation, or HE for each of the electrical field components $[\psi(x,y,z)]$:

$$\begin{gathered}\frac{\partial^2\psi(x,y,z)}{\partial x^2}+\frac{\partial^2\psi(x,y,z)}{\partial y^2}+\frac{\partial^2\psi(x,y,z)}{\partial z^2}+k_H^2\cdot\psi(x,y,z)=0\\ k_H=\frac{\omega}{c}\cdot\sqrt{\epsilon_H}\equiv k_0\cdot\sqrt{\epsilon_H}\equiv\frac{2\cdot\pi}{\lambda_0}\cdot\sqrt{\epsilon_H}\end{gathered} \tag{3}$$

where $k_H\equiv k_0\cdot\sqrt{\epsilon_H}$ is the free space wave number, i.e., the (possibly complex) wave number of a monochromatic wave of angular frequency ω, propagating through a homogeneous permittivity space.

Similar derivation holds for the magnetic field components (Yariv & Yeh, 1984), so that HE (Equation 3) holds for all six components of the electromagnetic field.

A common way of solving Equation (3) is using the separation of variables method (Tikhonov & Samarskii, 2011; Willatzen & Lew Yan Voon, 2011). Throughout this review, we adopt the common convention of assigning z to be the propagation (axial) axis and assume for the separation of variables: $\psi(q_x,q_y,z)=U(q_x,q_y)\cdot e^{i\cdot k_z\cdot z}$, where (q_x,q_y) are the transverse coordinates. Under this assumption, the three-dimensional HE (Equation 3) is reduced to a two-dimensional HE:

$$\begin{gathered}\psi(q_x,q_y,z)=U(q_x,q_y)\cdot e^{i\cdot k_z\cdot z}\\ \nabla_t^2\left[U(q_x,q_y)\right]+k_t^2\cdot U(q_x,q_y)=0\\ k_z(k_t)=\left[k_H^2-k_t^2\right]^{\frac{1}{2}}\end{gathered} \tag{4}$$

We refer to the separation of variables constant (k_t) in Equation (4) as the *transverse wave number*.

The four sets of Wave patterns discussed below are the sets of solutions to Equation (4) in four different systems of transverse coordinates.

Note, however, that the electric–magnetic field components are related to each other through Maxwell's equations. They can NOT all be calculated independently as solutions to HE (Equation 3). One rigorous way to

compute all six components of the free space electric–magnetic fields is to first construct, based on (one of the) solutions of HE (Equation 3), a vector known as the vector potential (Feynman, Leighton, & Sands, 1964; Konopinski, 1978), or more generally to construct two vector fields (Stratton, 1941, p. 394, equations 11 and 12). Then, from the constructed vector potential or from the constructed vector fields, derive the desired electric–magnetic field components (Levy & Silberberg, 2015; Volke-Sepulveda & Eugenio, 2006). Another way to calculate the electric–magnetic field components is to independently define two of the six components, using angular spectrums functions, and then obtain the remaining components from Maxwell's equations (Turunen & Friberg, 2009).

Note also that the free space electric–magnetic fields are generally NOT perpendicular to each other (Levy & Silberberg, 2015).

1.2 Beams

Beams are solutions of the paraxial HE discussed below. In this section of the review, we present the equation for Beams and, following Gutiérrez-Vega and Bandres (2005), discuss a special solution class—a class of wave-originated Gaussian Beams.

1.2.1 Equation

Beams are the solutions of a slowly varying envelope approximation-paraxial wave equation (SVEA-PWE) version of the full HE (Equation 3, Goodman, 1988; Kogelnik & Li, 1966):

$$\begin{gathered}\psi\left(q_x, q_y, z\right) \equiv \mathcal{F}\left(q_x, q_y, z\right) \cdot e^{i \cdot k_H \cdot z} \\ \nabla_t^2\left[\mathcal{F}\left(q_x, q_y, z\right)\right] + i \cdot 2 \cdot k_H \cdot \frac{\partial \mathcal{F}\left(q_x, q_y, z\right)}{\partial z} = 0\end{gathered} \tag{5}$$

Note that contribution to axial phase accumulation will come not only from the $k_H \cdot z$ product but also from the z-dependent phase contributed by the solution to the SVEA-PWE (Equation 5). In fact, in some cases, the axial phase accumulation will no longer be a straight line (cf. Figure 8).

1.2.2 Wave-Originated Gaussian Beams Solution

It was shown by Gutiérrez-Vega and Bandres (2005) that if $U[q_x(x,y), q_y(x,y); k_t]$ is a solution of the transverse HE (Equation 4), then

$$\begin{aligned}
&\psi\left[q_x(x,y),q_y(x,y),z\right] \\
&\equiv e^{-i\cdot\frac{k_t^2 z}{2\cdot k_H \mu}}\cdot GB(x,y,z)\cdot U\left[q_x\left(\frac{x}{\mu},\frac{y}{\mu}\right),q_y\left(\frac{x}{\mu},\frac{y}{\mu}\right);k_t\right] \\
&GB(x,y,z)\equiv\frac{1}{\mu}\cdot e^{i\cdot k_H\cdot z}\cdot e^{-\frac{x^2+y^2}{\mu\cdot\omega_0^2}} \\
&\mu=\mu(z)\equiv 1+i\cdot\frac{z}{z_R};z_R\equiv\frac{1}{2}\cdot k_H\cdot\omega_0^2
\end{aligned} \tag{6}$$

is a solution of the SVEA-PWE (Equation 5). Thus, the four patterns of Waves (solving **HE** (Equation 4) in different coordinate systems) "give birth" to four patterns of Beams [solving the **SVEA-PWE** (Equation 5)].

1.3 Classification

The variety of Waves and Beams, some of which were already reviewed in the literature (see, e.g., Korotkova, 2013) calls for classification. Here, as stated above, we divide the free space light patterns into two groups according to the governing equation they solve (columns of Table 1), and into four subgroups according to the related coordinate system (rows of Table 1). The Beams in blue (dark gray in the print version) fonts in Table 1 originate from the respective Waves listed to their left (cf. Equation 6).

1.4 Orthogonality and Completeness

Important properties, perhaps the most important properties, from a theoretical point of view as well as from a practical point of view, of the light-pattern sets listed in Table 1, are their orthogonality and completeness. As both HE (Equation 4) and SVEA-PWE (Equation 5) are solved by separation of variables, the resulting one-dimensional equations are of the Sturm–Liouville problem type (although not *regular*), with the separation constants as the eigenvalues (Morse & Feshbach, 1953; Tikhonov & Samarskii, 2011). Thus, each set of solutions to both HE (Equation 4) and SVEA-PWE (Equation 5) possesses orthogonality and completeness. For several sets listed in Table 1, the results concerning orthogonality and completeness are known in the literature (Freise & Kenneth, 2010; Forbes, 2014; Hernandez-Aranda, Gutiérrez-Vega, Guizar-Sicairos, & Bandres, 2006; Soifer, 2014). In particular, in Forbes (2014), the orthogonality and

Table 1 Classification of Light Patterns Propagating in Free Space

Coordinate System	Waves (Helmholtz Eq.)	Beams (SVEA-PWE)
Cartesian	A. Plane Waves (PWV)	E. Plane Infinite Beams (PIB) F. Airy Infinite Beams (AiI) G. Airy Finite Beams (AiF) H. Airy–Airy Beams (AAB) I. Airy–Plane Beams (APB) J. Hermite–Gauss Beams (HGB) K. Plane–Gauss Beams (PGB)
Circular–Cylindrical (Polar)	B. Bessel Waves (BSL)	L. Laguerre–Gauss Beams (LGB) M. Bessel–Gauss Beams (BGB)
Parabolic–Cylindrical	C. Weber Waves (WBR)	N. Parabolic Infinite Beams (PaI) O. Parabolic Finite Beams (PaF) P. Weber–Gauss Beams (WGB)
Elliptical–Cylindrical	D. Mathieu Waves (MTH)	Q. Ince–Gauss Beams (IGB) R. Mathieu–Gauss Beams (MGB)

The four Waves (center column) are solutions of the exact HE (Equation 4) in the respective coordinate system. The 14 Beams (right column) are solutions of the SVEA-PWE (Equation 5) in the respective coordinate system. The Beams in blue (dark gray in the print version) fonts originate from the respective Waves (cf. Equation 6).

completeness of *plane wave slices* are proven. Rodríguez-Lara (2010) presented explicit expressions for decomposition of Weber Waves into Bessel Waves and into Mathieu Waves (of the same transverse wave number (k_t)) based on the completeness of the latter sets.

General expressions for orthogonality and completeness are presented below.

1.4.1 Orthogonality

Associated with the two transverse coordinates (for both HE (Equation 4) and SVEA-PWE (Equation 5)) are two sets of eigenvalues (a_x, a_y). Two functions of a given solution set that belong to different eigenvalue pairs are orthogonal:

$$\iint_{\Omega_q} U\left(q_x, q_y; a_x, a_y\right) \cdot U^*\left(q_x, q_y; \grave{a}_x, \grave{a}_y\right) \cdot \mathrm{d}q_x \cdot \mathrm{d}q_y = C_q \cdot \delta\left(a_x - \grave{a}_x\right) \cdot \delta\left(a_y - \grave{a}_y\right) \tag{7}$$

where $\delta(\cdot)$ is a Dirac delta function and $\left[\left(a_x, a_y\right); \left(\grave{a}_x, \grave{a}_y\right)\right]$ are the sets of eigenvalues (discrete or continuous) of the equation (typically the separation constants). The integration area ($\boldsymbol{\Omega}_\mathrm{q}$) is the entire (here infinite) transverse plane.

1.4.2 Completeness

Completeness is assured if (Forbes, 2014, and only if) the integral over the eigenvalue space (or the sum in the case of a discrete set of eigenvalues) at two different spatial points $[(q_x, q_y),(\grave{q}_x, \grave{q}_y)]$ vanishes:

$$\iint_{\boldsymbol{\Omega}_\mathrm{a}} U\left(q_x, q_y; a_x, a_y\right) \cdot U^*\left(\grave{q}_x, \grave{q}_y; a_x, a_y\right) \cdot \mathrm{d}a_x \cdot \mathrm{d}a_y = C_a \cdot \delta(q_x - \grave{q}_x) \cdot \delta\left(q_y - \grave{q}_y\right). \tag{8}$$

The integration range ($\boldsymbol{\Omega}_\mathrm{a}$) is the entire eigenvalue space. Given Equation (8), any square-integrable function (any *input* field, $F(q_x, q_y)$) defined over the transverse plane, can be accurately reconstructed (expanded) by the set of the solution functions:

$$F\left(q_x, q_y\right) = \iint_{\boldsymbol{\Omega}_\mathrm{a}} C_{a_x, a_y} \cdot U\left(q_x, q_y; a_x, a_y\right) \cdot \mathrm{d}a_x \cdot \mathrm{d}a_y \tag{9}$$

with expansion coefficients (C_{a_x, a_y}) given by

$$C_{a_x, a_y} = \iint_{\boldsymbol{\Omega}_\mathrm{q}} F\left(q_x, q_y\right) \cdot U^*\left(q_x, q_y; a_x, a_y\right) \cdot \mathrm{d}q_x \cdot \mathrm{d}q_y \tag{10}$$

Completeness of the plane infinite beams (E in Table 1), for example, is the basis for (paraxial) Fourier optics (Goodman, 1988).

Below, we illustrate set-completeness by one-dimensional the *Airy transform*.

1.4.3 Example: Gaussian Propagation by the Airy Transform

Airy functions (cf. Section 3.1.2) make a convenient complete basis set. Much like plane wave functions (cf. Section 3.1.1), Airy functions are one-dimensional (counting transverse coordinates only) and are associated with a continuous set of eigenvalues.

In the example illustrated in Figure 1, we compare the *Airy transform* to Fourier transform. We use both transforms to decompose a one-dimensional Gaussian (the input field) into the respective base functions, propagate the base functions a certain axial distance (z), and recompose (perform the inverse

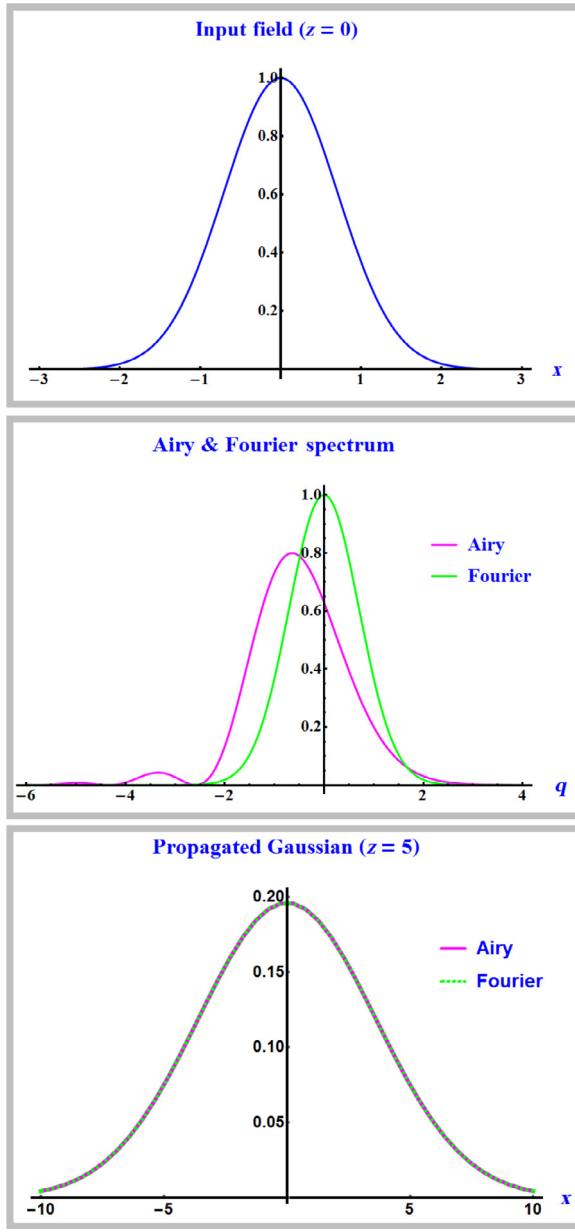

Figure 1 Comparing the Airy transform to Fourier transform (cf. Equations 9 and 10). The scenario of the Airy transform and a Gaussian input is just an example. Any square-integrable function (the input field) defined over the transverse plane, can be accurately expanded (and propagated) by each of the function sets listed in Table 1. *Note*: here x, q, and z are dimensionless.

transform) to get the resulted diffraction pattern. Both transforms indeed yield the same diffraction pattern (expanded Gaussian in this specific example).

1.5 Countability

Each of the Wave and Beam function sets listed in Table 1 is associated with two sets of eigenvalues (typically the separation constants). These eigenvalue sets, by which the different Wave and Beam functions are identified (counted), can be discrete (i.e., *countable*) or continuous. In Table 2, we classify the Wave and Beam sets according to their countability.

1.6 Diffraction Characteristics

As a single Wave (one pair of eigenvalues) or a single Beam (one pair of eigenvalues) of Table 1 propagates along the axial (z) direction, changes in the intensity pattern (relative to the intensity pattern at $z = 0$) may or may not occur.

In Table 3, we have classified Waves and Beams according to their diffraction characteristics. Following is a brief explanation of the terms listed along the left (*Diffraction Properties*) column.

1.6.1 No Diffraction

Intensity patterns at all axial distances are equal. Waves, as Table 3 shows, do not diffract. In fact, any combination of waves associated with a fixed

Table 2 Countability of Wave and Beam Sets

Countability	Waves	Beams
Continuous/ continuous	Plane Waves Weber Waves	Plane Infinite Beams Airy Infinite Beams Airy Finite Beams Airy–Airy Beams Airy–Plane Beams Plane–Gauss Beams Weber–Gauss Beams
Continuous/ countable	Bessel Waves Mathieu Waves	Bessel–Gauss Beams Parabolic Infinite Beams Parabolic Finite Beams Mathieu–Gauss Beams
Countable/ countable		Hermite–Gauss Beams Laguerre–Gauss beams Ince–Gauss Beams

Decomposition of input fields into each of these function sets is a two-dimensional integral (top row—cf. Equation 9) or a double-index sum (bottom row) or a combination (middle row).

Table 3 Diffraction Properties of the Waves and Beams Listed in Table 1

Diffraction Properties	Waves	Beams
No diffraction	Plane Waves Bessel Waves Weber Waves Mathieu Waves	Plane Infinite Beams
Expansion		Hermite–Gauss Beams Laguerre–Gauss beams Ince–Gauss Beams
Acceleration		Airy Infinite Beams Airy–Airy Beams Airy–Plane Beams Parabolic Infinite Beams
Acceleration and slow diffraction		Airy Finite Beams Parabolic Finite Beams
Diffraction		Plane–Gauss Beams Bessel–Gauss Beams Weber–Gauss Beams Mathieu–Gauss Beams

See text for discussion of the terms in the left column.

transverse wave number (k_t) does not diffract. As all waves in the combination accumulate axial phase at the same rate, the pattern remains unchanged (Gutiérrez-Vega et al., 2000; cf. Equation 11).

1.6.2 Expansion

The intensity pattern at a certain transverse plane is a scaled copy of the pattern at any other transverse plane. Scales in the x-direction and y-direction can generally be different (i.e., aspect ratio is not generally preserved).

1.6.3 Acceleration

Intensity patterns can shift transversely. The shift rate $[x(z); y(z)]$ is parabolic with axial distance (hence *acceleration*). Other than a transverse shift, the intensity pattern remains unchanged.

1.6.4 Acceleration and Slow Diffraction

Intensity patterns accelerate and in addition gradually change. The rate of change is dictated by the value of an *attenuation parameter* (cf. Sections 3.1.3 and 3.3.2).

1.6.5 Diffraction

Intensity patterns generally do change with axial distance. As listed in Table 3, all wave-originated Wave–Gauss Beams do diffract. They diffract in one of the two modes (Gori, Guattari, & Padovani, 1987): a slow-expansion mode [$\omega_0 < 2/k_t$] or a fast-expansion mode [$\omega_0 > 2/k_t$]. In the slow-expansion mode, the pattern due to a slow expanding wave (small k_t) remains under a (relatively fast-expanding) centered Gaussian. This mode alone could have been classified under *expansion*. In the fast-expansion mode, the pattern due to a fast expanding wave (large k_t) is seen under (modulated by) a Gaussian ring (gradually formed during propagation).

These two diffraction modes of Wave–Gauss Beams, along with an intermediate mode, are illustrated in Figure 2. And whereas the curves in the figure are calculated for Plane–Gauss Beams, the same diffraction modes characterize all four Wave–Gauss Beams (see Figures 14, 16, 19, and 21).

This discussion on diffraction characteristics ends the overview section. We move now to presenting, one-by-one, mathematical equations, and typical intensity patterns of all Waves and Beams listed in Table 1, starting with Waves.

2. WAVES

Waves are solutions of the HE (Equation 4) in Cartesian coordinates and in three *Transverse-Cylindrical* coordinate systems. Before treating the individual Waves, let's briefly elaborate on their nondiffracting feature. One of the two eigenvalues associated with all four Waves (directly or indirectly) is the transverse wave number (k_t). Combinations of Waves with a fixed transverse wave number do not diffract. It clearly follows from the angular spectrum equation displayed in the next subsection. Note that when a given input field is decomposed into one of the Wave sets, the transverse wave number (k_t) is NOT generally fixed, and the input field WILL generally diffract as expected.

2.1 Angular Spectrum

The PIOFs were discussed by Gutiérrez-Vega et al. (2000), where the authors started with an angular spectrum equation (Stratton, 1941, section 7.7—equation 58; Durnin, 1987) given by (slightly modified) Equation (11):

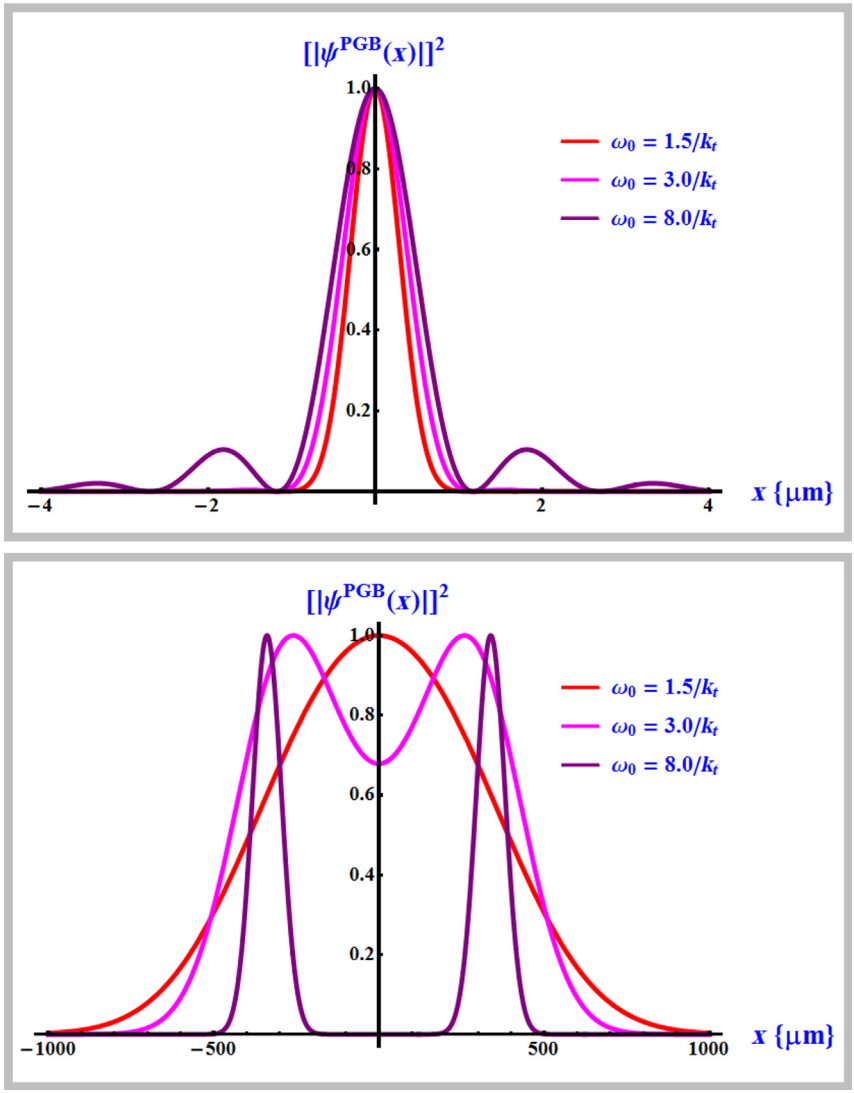

Figure 2 Propagation modes of Wave–Gauss Beams (marked by blue (dark gray in the print version) fonts in Table 1). The figure shows three $(x,y=0)$ cross sections of a Plane–Gauss Beam (cf. Section 3.1.7), made of superposition of seven Plane Waves equally spaced on the azimuthal circle, under a centered Gaussian (cf. Figure 14). Top: $z=0$. Bottom: $z=2000\mu m$ $\{k_t \approx 2(\mu m)^{-1}\}$. Looking at the bottom curves, in the slow-expansion mode $[\omega_0 < 2/k_t]$, the pattern remains under a centered Gaussian (red (gray in the print version)). In the fast-expansion mode $[\omega_0 > 2/k_t]$, the pattern is seen under (modulated by) a Gaussian ring (purple (dark gray in the print version)). See Figures 14, 16, 19, and 21).

$$x(q_x, q_y); y(q_x, q_y)\psi(q_x, q_y, z) = \exp(i \cdot k_z \cdot z) \cdot \int_0^{2\cdot\pi} A(\varphi) \cdot \left[\exp\left\{i \cdot k_t \cdot \left[x(q_x, q_y) \cdot \cos(\varphi) + y(q_x, q_y) \cdot \sin(\varphi)\right]\right\}\right] \cdot \mathrm{d}\varphi \tag{11}$$

with $A(\varphi)$ being the (complex) angular spectrum. It was also remarked by Gutiérrez-Vega et al. (2000), that Equation (11) *is the solution of the HE in any cylindrical coordinate system by performance of the corresponding coordinate transformation*. In the context of this review—the four Waves.

Let us zoom-in now and describe each of the four Waves in detail.

2.2 Cartesian Coordinates: Plane Waves

To solve the HE (Equation 4) in Cartesian coordinates, a next step of variable separation is performed:

$$\begin{gathered} q_x \longrightarrow x \in (-\infty, \infty); q_y \longrightarrow y \in (-\infty, \infty) \\ U(x, y) = \mathbb{U}_x(x) \cdot \mathbb{V}_y(y), \end{gathered} \tag{12}$$

leading to a set of two equations (and one governing condition),

$$\begin{gathered} \frac{1}{\mathbb{U}_x(x)} \cdot \frac{\mathrm{d}^2\mathbb{U}_x(x)}{\mathrm{d}x^2} = -k_x^2 \\ \frac{1}{\mathbb{V}_y(y)} \cdot \frac{\mathrm{d}^2\mathbb{V}_y(y)}{\mathrm{d}y^2} = -k_y^2 \\ -\left(k_x^2 + k_y^2\right) + k_t^2 = 0 \end{gathered} \tag{13}$$

The solution to Equation (13) is given by:

$$\begin{gathered} \mathbb{U}_x(x) = A_x \cdot e^{i \cdot k_x \cdot x} + B_x \cdot e^{-i \cdot k_x \cdot x} \\ \mathbb{V}_y(y) = A_y \cdot e^{i \cdot k_y \cdot y} + B_y \cdot e^{-i \cdot k_y \cdot y} \\ -\left(k_x^2 + k_y^2\right) + k_t^2 = 0 \end{gathered} \tag{14}$$

The general solution to HE (Equation 4) in Cartesian coordinates $[\psi^{PWV}(x, y, z; k_x, k_y)]$ is thus:

$$\begin{gathered} \Longrightarrow \psi^{PWV}(x, y, z; k_x, k_y) = \left(A_x \cdot e^{i \cdot k_x \cdot x} + B_x \cdot e^{-i \cdot k_x \cdot x}\right) \cdot \\ \left(A_y \cdot e^{i \cdot k_y \cdot y} + B_y \cdot e^{-i \cdot k_y \cdot y}\right) \cdot e^{i \cdot k_z \cdot z}; -\left(k_x^2 + k_y^2 + k_z^2\right) + k_H^2 = 0 \end{gathered} \tag{15}$$

Two comments are pertinent here. The first comment is related to the allowed values of the eigenvalues (k_x, k_y) that can be real or imaginary

leading to oscillating or exponentially growing (or decaying) solutions, provided that Equations (13) are satisfied. In this review, we concentrate on physical, i.e., bounded solutions, and ignore nonphysical (even if mathematically allowed) solutions.

The second comment is related to the countability (actually uncountability) of the eigenvalues ((k_x, k_y) in Equation 13): the allowed range for each of the eigenvalues is continuous (Tikhonov & Samarskii, 2011). A general solution that satisfies the initial conditions (typically a square-integrable input field at $z = 0$), is given by a two-dimensional integral of the solutions given in (14).

Example of an intensity pattern (nondiffracting) that results from a superposition of Plane Waves having the same transverse wave number ((k_t), Equation 16) is shown in Figure 3.

Shown in Figure 3 is the following superposition of Plane Waves:

$$\begin{gathered}\psi^{PWV}(x, y; k_t) = \sum_{n=1}^{5} e^{i \cdot k_t \cdot \sin[(n-1)\cdot\phi]\cdot x} \cdot e^{i \cdot k_t \cdot \cos[(n-1)\cdot\phi]\cdot y} \\ \phi = \frac{2\cdot\pi}{5};\ \lambda_0 = 0.8\,\mu\text{m};\ n_H = 1.5;\ \theta = \frac{\pi}{6};\ k_H = \frac{2\cdot\pi\cdot n_H}{\lambda_0}(\mu\text{m})^{-1} \\ k_t = k_H \cdot \sin(\theta)(\mu\text{m})^{-1}\end{gathered} \tag{16}$$

Throughout this review, we adhere to the parameters of Equation (16) with axial angle, where relevant, in the range $0 < \theta \leq \pi/6$.

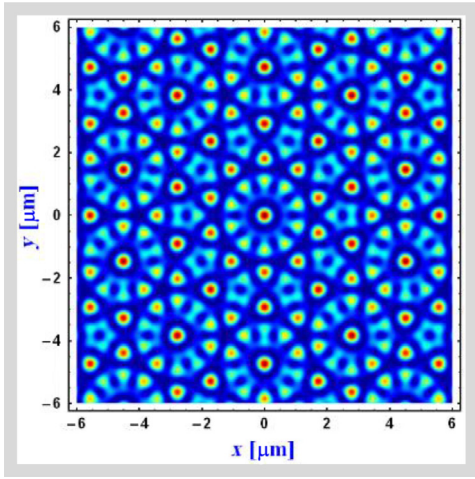

Figure 3 Intensity pattern due to a superposition of Plane Waves (Equation 16). The pattern is nondiffracting.

2.3 Circular–Cylindrical Coordinates: Bessel Waves

The well-known Bessel Waves are solutions of the HE (Equation 4) in circular–cylindrical coordinates (Arfken, Weber, & Harris, 2012, chapter 9.6):

$$\begin{gathered} q_x \longrightarrow \rho \in [0,\infty);\ q_y \longrightarrow \varphi \in [0, 2\cdot\pi) \\ x = \rho\cdot\cos(\varphi);\ y = \rho\cdot\sin(\varphi) \\ U(\rho,\varphi) = \mathbb{U}_\rho(\rho)\cdot\mathbb{V}_\varphi(\varphi) \end{gathered} \tag{17}$$

The two-dimensional HE (Equation 4) splits now into two one-dimensional equations:

$$\begin{gathered} \frac{1}{\mathbb{V}_\varphi(\varphi)}\cdot\frac{\mathrm{d}^2\mathbb{V}_\varphi(\varphi)}{\mathrm{d}\varphi^2} = -l^2 \\ \frac{1}{\mathbb{U}_\rho(\rho)}\cdot\left\{\rho^2\cdot\frac{\mathrm{d}^2\mathbb{U}_\rho(\rho)}{\mathrm{d}\rho^2} + \rho\cdot\frac{\mathrm{d}\mathbb{U}_\rho(\rho)}{\mathrm{d}\rho}\right\} + k_t^2\cdot\rho^2 = l^2 \end{gathered} \tag{18}$$

Solutions to the top Equation (18) are of course $e^{\pm i\cdot l\cdot\varphi}$. To ensure a physical (i.e., periodic) solution, l must be an integer ($l = 0, 1, 2, \ldots$).

Thus, the physical solutions to Equations (18) (dropping the nonphysical Bessel functions of the second kind) are:

$$\begin{gathered} \mathbb{V}_\varphi(\varphi) = A_l\cdot e^{i\cdot l\cdot\varphi} + B_l\cdot e^{-i\cdot l\cdot\varphi};\ l = 0, 1, 2\ldots \\ \mathbb{U}_\rho(\rho) = C_l\cdot J_l(k_t\cdot\rho) \end{gathered} \tag{19}$$

The general physical solution to HE (Equation 4) in circular–cylindrical coordinates $[\psi^{BSL}(\rho,\varphi,z;k_t,l)]$ is thus:

$$\psi^{BSL}(\rho,\varphi,z;k_t,l) = J_l(k_t\cdot\rho)\cdot\left(A_l\cdot e^{i\cdot l\cdot\varphi} + B_l\cdot e^{-i\cdot l\cdot\varphi}\right)\cdot e^{i\cdot k_z\cdot z} \tag{20}$$

Examples of frequently encountered intensity patterns (nondiffracting) of Bessel Waves with two different eigenvalue pairs (k_t, l) are shown in Figure 4.

2.4 Parabolic–Cylindrical Coordinates: Weber Waves

In parabolic–cylindrical coordinates:

$$\begin{gathered} q_x \longrightarrow \eta \in (-\infty,\infty);\ q_y \longrightarrow \xi \in [0,\infty) \\ x + i\cdot y = \frac{(\eta + i\cdot\xi)^2}{2} \\ U(\eta,\xi) = \mathbb{U}_\eta(\eta)\cdot\mathbb{V}_\xi(\xi), \end{gathered} \tag{21}$$

the two-dimensional HE (Equation 4) splits by separation of variables into two one-dimensional equations:

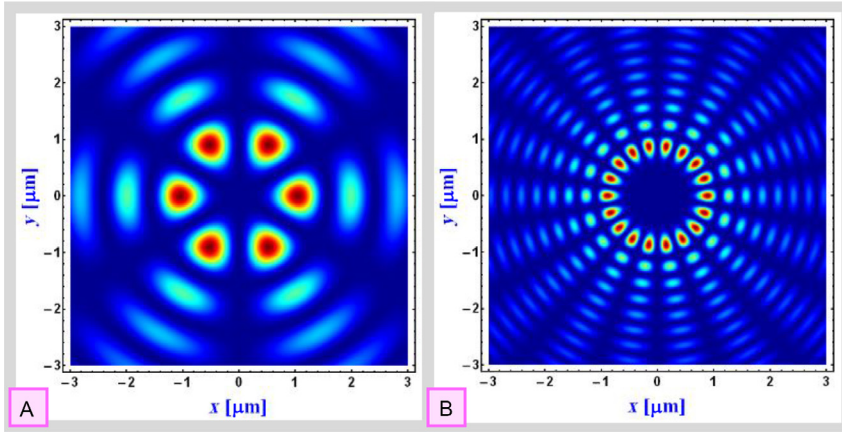

Figure 4 Intensity patterns due to Bessel Waves (Equation 20) with two different eigenvalue pairs (k_t, l). The patterns are nondiffracting.

$$\begin{aligned}\frac{1}{\mathbb{U}_\eta(\eta)}\cdot\frac{\mathrm{d}^2\mathbb{U}_\eta(\eta)}{d\eta^2}+k_t^2\cdot\eta^2&=-2\cdot k_t\cdot a\\ \frac{1}{\mathbb{V}_\xi(\xi)}\cdot\frac{\mathrm{d}^2\mathbb{V}_\xi(\xi)}{d\xi^2}+k_t^2\cdot\xi^2&=+2\cdot k_t\cdot a\end{aligned}\tag{22}$$

The separation of variables constant $(2\cdot k_t\cdot a)$ was written in this way for convenience (Bandres et al., 2004).

Nondiffracting parabolic waves, or Weber Waves, which are the solutions to Equations (22), can be presented as an infinite series (Bandres et al., 2004). Here, we present the solution via even and odd hypergeometric functions (Abramowitz & Stegun, 1964; Banders & Rodríguez-Lara, 2013; Rodríguez-Lara, 2010):

Even:

$$\begin{aligned}\mathbb{U}_{\eta,e}(\eta;a,k_t)&=e^{-\frac{i\cdot k_t\cdot\eta^2}{2}}\cdot{}_1F_1\left[\frac{1}{4}-\frac{i\cdot a}{2},\frac{1}{2},i\cdot k_t\cdot\eta^2\right]\\ \mathbb{V}_{\xi,e}(\xi;a,k_t)&=e^{-\frac{i\cdot k_t\cdot\xi^2}{2}}\cdot{}_1F_1\left[\frac{1}{4}+\frac{i\cdot a}{2},\frac{1}{2},i\cdot k_t\cdot\xi^2\right]\end{aligned}$$

Odd:

$$\begin{aligned}\mathbb{U}_{\eta,o}(\eta;a,k_t)&=\sqrt{2\cdot k_t}\cdot\eta\cdot e^{-\frac{i\cdot k_t\cdot\eta^2}{2}}\cdot{}_1F_1\left[\frac{3}{4}-\frac{i\cdot a}{2},\frac{3}{2},i\cdot k_t\cdot\eta^2\right]\\ \mathbb{V}_{\xi,o}(\xi;a,k_t)&=\sqrt{2\cdot k_t}\cdot\xi\cdot e^{-\frac{i\cdot k_t\cdot\xi^2}{2}}\cdot{}_1F_1\left[\frac{3}{4}+\frac{i\cdot a}{2},\frac{3}{2},i\cdot k_t\cdot\xi^2\right]\end{aligned}\tag{23}$$

The general solution to the HE (Equation 4) in parabolic–cylindrical coordinates $[\psi^{WBR}(\eta, \xi, z; a, k_t)]$ is thus:

$$\psi^{WBR}(\eta, \xi, z; a, k_t) = \left(A_e \cdot \mathbb{U}_{\eta,e}(\eta; a, k_t) + A_o \cdot \mathbb{U}_{\eta,o}(\eta; a, k_t)\right) \cdot \left(B_e \cdot \mathbb{V}_{\xi,e}(\xi; a, k_t) + B_o \cdot \mathbb{V}_{\xi,o}(\xi; a, k_t)\right) \cdot e^{i \cdot k_z \cdot z} \tag{24}$$

Zhang et al. (2012) indeed constructed forward propagating Weber Waves by selecting specific values for the coefficients in (24). Nondiffracting intensity patterns due to Weber Waves (Equation 24) are displayed in Figure 5.

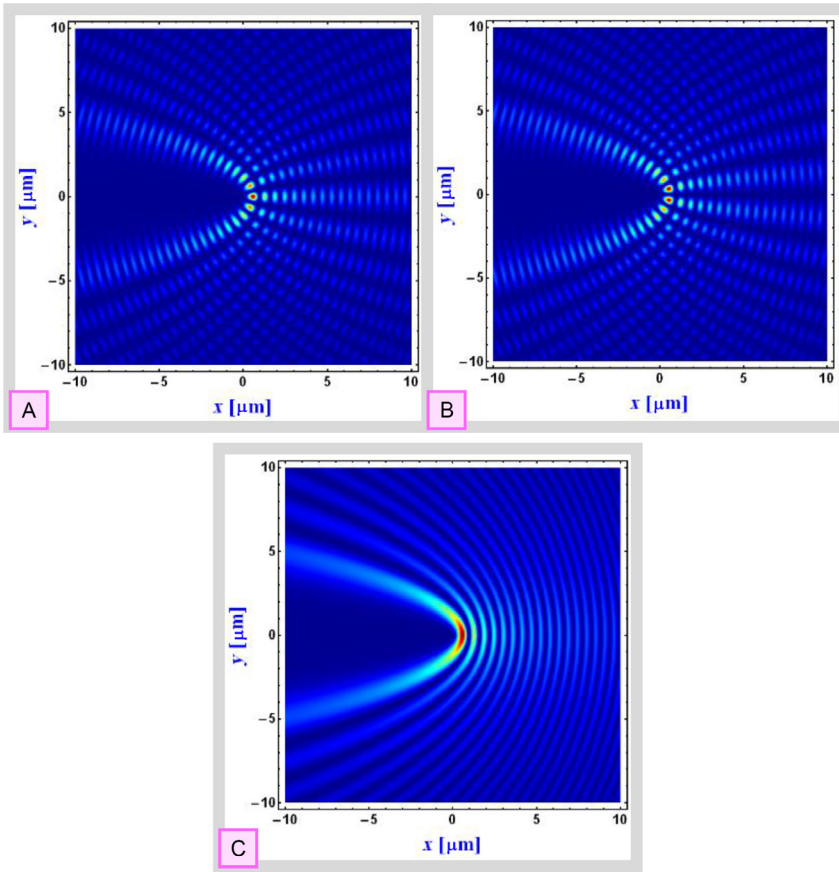

Figure 5 Intensity patterns due to Weber Waves (Equation 24). (A) Even. (B) Odd. (C) Equal-weight combination (Rodríguez-Lara, 2009). The patterns are nondiffracting.

2.5 Elliptical–Cylindrical Coordinates: Mathieu Waves

In elliptical–cylindrical coordinates:

$$\begin{gathered} q_x \longrightarrow \zeta \in [0,\infty);\ q_y \longrightarrow \phi \in [0, 2\cdot\pi) \\ x = f_0 \cdot \cosh(\zeta) \cdot \cos(\phi);\ y = f_0 \cdot \sinh(\zeta) \cdot \sin(\phi) \\ U(\zeta,\varphi) = \mathbb{U}_\zeta(\zeta) \cdot \mathbb{V}_\phi(\phi), \end{gathered} \tag{25}$$

the two-dimensional HE (Equation 4) splits by separation of variables into two one-dimensional equations:

$$\begin{gathered} \frac{1}{\mathbb{V}_\phi(\phi)} \cdot \frac{\mathrm{d}^2\mathbb{V}_\phi(\phi)}{d\phi^2} - \frac{k_t^2 \cdot h^2}{2} \cdot \cos(2\cdot\phi) = -\lambda_t \\ \frac{1}{\mathbb{U}_\zeta(\zeta)} \cdot \frac{\mathrm{d}^2\mathbb{U}_\zeta(\zeta)}{d\zeta^2} + \frac{k_t^2 \cdot h^2}{2} \cdot \cosh(2\cdot\zeta) = \lambda_t \end{gathered} \tag{26}$$

Let us define a dimensionless parameter Q_t as

$$Q_t \equiv \frac{k_t^2 \cdot h^2}{4} \tag{27}$$

and write (26) in its classical form (Equation 28), the top one known as the *canonical form of Mathieu's differential equation* (Abramowitz & Stegun, 1964) or as *angular Mathieu differential equation* (Gutiérrez-Vega, Rodrigez-Dagnino, Meneses-Nava, & Chavez-Cerda, 2003); and the bottom one is known as *modified Mathieu's differential equation* (Abramowitz & Stegun, 1964) or as *radial Mathieu differential equations* (Gutiérrez-Vega et al., 2003):

$$\begin{gathered} \frac{\mathrm{d}^2\mathbb{V}_\phi(\phi)}{d\phi^2} + [\lambda_t - 2\cdot Q_t \cdot \cos(2\cdot\phi)] \cdot \mathbb{V}_\phi(\phi) = 0 \\ \frac{\mathrm{d}^2\mathbb{U}_\zeta(\zeta)}{d\zeta^2} - [\lambda_t - 2\cdot Q_t \cdot \cosh(2\cdot\zeta)]\mathbb{U}_\zeta(\zeta) = 0 \end{gathered} \tag{28}$$

Solutions to the canonical form of Mathieu's differential equation (top of Equation 28) are linear superpositions of

$$\begin{gathered} \mathit{Mathieu}\ C\left[\lambda_{t,a}, Q_t, \phi\right]\{\mathit{even}\} \\ \mathit{Mathieu}\ S\left[\lambda_{t,b}, Q_t, \phi\right]\{\mathit{odd}\} \end{gathered} \tag{29}$$

where *Mathieu C* is an even Mathieu function with characteristic value $\lambda_{t,a}$ and parameter Q_t; and *Mathieu S* is an odd Mathieu function with characteristic value $\lambda_{t,b}$ and parameter Q_t.

Solutions to the Mathieu's modified differential equation (the bottom Equation 28) are linear superpositions of

$$\begin{aligned} &Mathieu\ C\left[\lambda_{t,a}, Q_t, i\cdot\zeta\right]\{even\} \\ &i\cdot Mathieu\ S\left[\lambda_{t,b}, Q_t, i\cdot\zeta\right]\{odd\} \end{aligned} \tag{30}$$

Note: Preceding "i" multiplication in the lower part of (30) results in a real target (i.e., target function values $\in \mathbb{R}$).

Characteristic values ($\lambda_{t,a}; \lambda_{t,b}$) are calculated to yield periodic solutions for the even/odd *Mathieu C*/*Mathieu S* functions (Abramowitz & Stegun, 1964). Given these characteristic values, we switch to the following short notations:

$$\begin{aligned} &Mathieu\ C\left[\lambda_{t,n}, Q_t, \phi\right] \longrightarrow ce_n(\phi; Q_t);\ n=0,1,\ldots, \\ &Mathieu\ S\left[\lambda_{t,n}, Q_t, \phi\right] \longrightarrow se_n(\phi; Q_t);\ n=1,2,\ldots, \end{aligned} \tag{31}$$

and

$$\begin{aligned} &Mathieu\ C\left[\lambda_{t,n}, Q_t, i\cdot\zeta\right] = ce_n(Q_t; i\cdot\zeta) \equiv Je_n(\zeta; Q_t);\ n=0,1,\ldots, \\ &-i\cdot Mathieu\ S\left[\lambda_{t,n}, Q_t, i\cdot\zeta\right] = -i\cdot se_n(Q_t; i\cdot\zeta) \equiv Jo_n(\zeta; Q_t) \\ &n=1,2,\ldots, \end{aligned} \tag{32}$$

The general solution to HE (Equation 4) in elliptical–cylindrical coordinates $[\psi^{MTH}(\zeta, \phi, z; \lambda_{t,n}, Q_t)]$ is a linear superposition of solutions (31) and (32):

$$\begin{aligned} \psi^{\mathrm{MTH}}\left(\zeta, \phi, z; \lambda_{t,n}, Q_t\right) = &\left[A_e\cdot ce_n(Q_t; \phi) + A_o\cdot se_n(Q_t; \phi)\right]\cdot \\ &\left[B_e\cdot Je_n(Q_t, \zeta) + B_o\cdot Jo_n(Q_t, \zeta)\right]\cdot e^{i\cdot k_z\cdot z} \end{aligned} \tag{33}$$

Nondiffracting intensity patterns due to Mathieu Waves (Equation 33) are displayed in Figure 6.

The shown Mathieu Waves intensity patterns (Figure 6) conclude our review of Waves. We proceed now to discussing the 14 types of Beams as listed in Table 1.

3. BEAMS

In this section, we bring forward the equations and sample intensity patterns for the 14 Beam sets listed in Table 1. Each set of Beams is a solution to the SVEA-PWE (Equation 5). The functions of each set are orthogonal (with respect to the eigenvalues—Equation 7), and each set is complete (Equations 8–10).

Four of the 14 Beam sets are wave-originated (Gutiérrez-Vega & Bandres, 2005, colored blue (dark gray in the print version) in Table 1). The Airy Finite Beams (Siviloglou & Christodoulides, 2007), and the

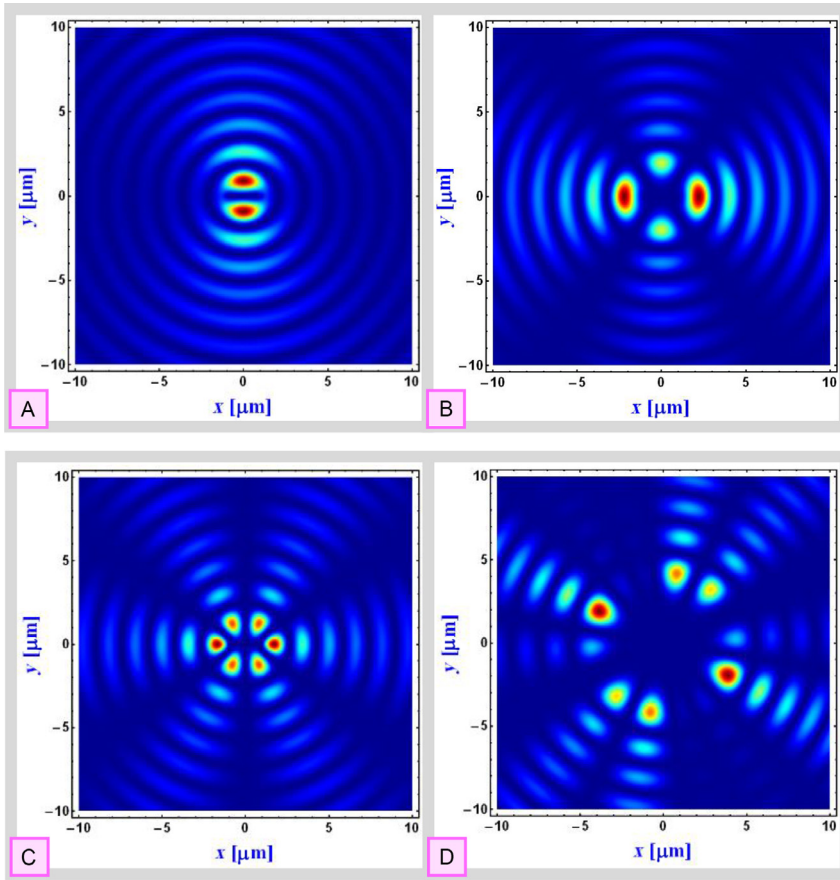

Figure 6 Intensity patterns due to Mathieu Waves (Equation 33). Increasing order (of the characteristic values) going from (A) to (C). (D) High order combination with $\lambda_{t,a} = 7; \lambda_{t,b} = 3$. The patterns are nondiffracting.

Parabolic Finite Beams (Bandres, 2008), are variants of their respective infinite sets, their construction is based on the translation invariance properties of the SVEA-PWE (Equation 5, Bandres, 2008).

Seven of the 14 Beam sets listed in Table 1 are solutions of SVEA-PWE (Equation 5) in Cartesian coordinates.

3.1 Cartesian Coordinates

Given now are Cartesian coordinates:

$$\begin{gathered} q_x \longrightarrow x \in (-\infty, \infty);\ q_y \longrightarrow y \in (-\infty, \infty) \\ \mathcal{F}(q_x, q_y, z) \longrightarrow \mathcal{F}(x, y, z). \end{gathered} \tag{34}$$

A first step of variables separation (of Equation 5) is performed (Banders & Gutiérrez-Vega, 2007; Siviloglou & Christodoulides, 2007) by introducing a trial solution:

$$\mathcal{F}(x, y, z) = \boldsymbol{\Phi}_x(x, z) \cdot \boldsymbol{\Phi}_y(y, z) \tag{35}$$

The SVEA-PWE (Equation 5) in Cartesian coordinates, under the trial solution (35), separates into:

$$\begin{aligned} \frac{\partial^2 \boldsymbol{\Phi}_x(x, z)}{\partial x^2} + i \cdot 2 \cdot k_H \cdot \frac{\partial \boldsymbol{\Phi}_x(x, z)}{\partial z} = 0 \\ \frac{\partial^2 \boldsymbol{\Phi}_y(y, z)}{\partial y^2} + i \cdot 2 \cdot k_H \cdot \frac{\partial \boldsymbol{\Phi}_y(y, z)}{\partial z} = 0 \end{aligned} \tag{36}$$

Equations (36) are solved by several distinct beam sets as follows.

3.1.1 Plane Infinite Beams

Probably, the simplest way of solving Equations (36) is yet another (second) step of variable separation:

$$\begin{aligned} \boldsymbol{\Phi}_x(x, z) = f_x(x) \cdot f_z(z) \\ \boldsymbol{\Phi}_y(y, z) = g_y(y) \cdot g_z(z) \end{aligned} \tag{37}$$

This second step yields:

$$\begin{aligned} i \cdot \frac{1}{f_z(z)} \cdot \frac{\mathrm{d} f_z(z)}{\partial z} = Q_x; \quad \frac{1}{2 \cdot k_H} \cdot \frac{1}{f_x(x)} \cdot \frac{\mathrm{d}^2 f_x(x)}{\partial x^2} = -Q_x \\ i \cdot \frac{1}{g_z(z)} \cdot \frac{\mathrm{d} g_z(z)}{\partial z} = Q_y; \quad \frac{1}{2 \cdot k_H} \cdot \frac{1}{g_y(y)} \cdot \frac{\mathrm{d}^2 g_y(y)}{\partial y^2} = -Q_y \end{aligned} \tag{38}$$

Let us define

$$\begin{aligned} k_x^2 \equiv 2 \cdot k_H \cdot Q_x \\ k_y^2 \equiv 2 \cdot k_H \cdot Q_y \end{aligned} \tag{39}$$

Now solve Equations (38) and through (37), (35) and top of (5), write the Plane Infinite Beams solution $[\psi^{PIB}(x, y, z; k_x, k_y)]$ to the SVEA-PWE (Equation 5) as

$$\begin{aligned}\mathcal{F}^{PIB}(x, y, z; k_x, k_y) = &\left(A_x \cdot e^{i \cdot k_x \cdot x} + B_x \cdot e^{-i \cdot k_x \cdot x}\right) \cdot \\ &\left(A_y \cdot e^{i \cdot k_y \cdot y} + B_y \cdot e^{-i \cdot k_y \cdot y}\right) \cdot \\ &e^{-i \cdot \left(Q_x + Q_y\right) \cdot z} \psi^{PIB}(x, y, z; k_x, k_y) \\ &\equiv \mathcal{F}^{PIB}(x, y, z; k_x, k_y) \cdot e^{i \cdot k_H \cdot z} \\ &\left\{ \Longrightarrow k_z \equiv k_H - \left(Q_x + Q_y\right) = k_H - \frac{k_x^2 + k_y^2}{2 \cdot k_H} \right\}\end{aligned} \tag{40}$$

The orthogonal and complete set of paraxial Plane Infinite Beams of Equation (40) is the basis of Fourier Optics (*Fresnel diffraction*, Goodman, 1988).

An example of an intensity pattern (nondiffracting) that results from a superposition of seven Plane Infinite Beams having the same transverse wave number ($(k_t^2 \equiv k_x^2 + k_y^2)$, cf. Equation (16) with five replaced by seven) is shown in Figure 7.

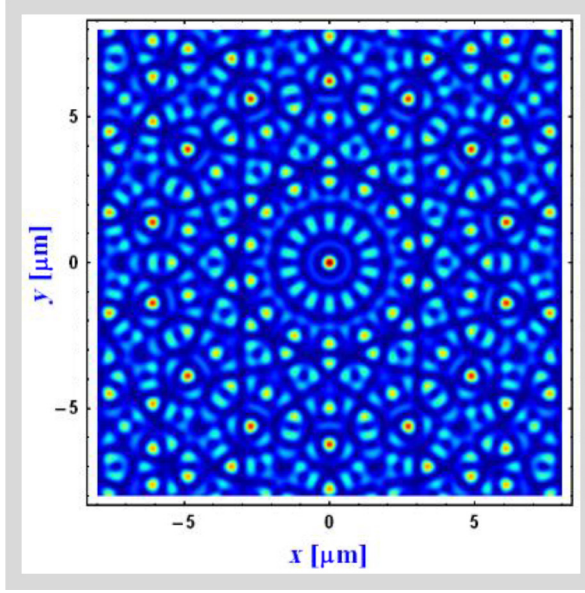

Figure 7 Intensity pattern due to a superposition of Plane Infinite Beams having the same transverse wave number ($(k_t^2 \equiv k_x^2 + k_y^2)$, cf. Equation 16 with five replaced by seven). The pattern is nondiffracting.

3.1.2 Airy Infinite Beams

Equations (36) are solved by Airy functions with an argument that is a combination of one transverse coordinate (x or y) and the axial coordinate (z). A nonspreading Airy wave packet was analyzed by Berry and Balazs (1979) in the context of a time-dependent Schrödinger equation (in one spatial coordinate). The one-dimensional Airy equation also appears in quantum mechanics in relation to a particle moving in a linear potential (Berberan-Santos, Bodunov, & Pogliani, 2005). Since their relatively recent introduction to the optics field (Siviloglou & Christodoulides, 2007), several groups studied the properties of Airy Beams and generated Airy Beams of various types (Banders & Gutiérrez-Vega, 2007; Broky, Siviloglou, Dogariu, & Christodoulides, 2008; Hu et al., 2012; Porat, Dolev, Barlev, & Arie, 2011; Siviloglou, Broky, Dogariu, & Christodoulides, 2007, 2008; Voloch-Bloch, Lereah, Lilach, Gover, & Arie, 2013; Zhang et al., 2012).

We start from Equations (36). Define the following dimensionless variables (Siviloglou & Christodoulides, 2007):

$$S_x \equiv \frac{x}{x_0};\ S_y \equiv \frac{y}{y_0};\ \xi_x \equiv \frac{z}{k_H \cdot x_0^2};\ \xi_y \equiv \frac{z}{k_H \cdot y_0^2} \tag{41}$$

To obtain

$$\begin{aligned} \frac{1}{2} \cdot \frac{\partial^2 \boldsymbol{\Phi}_x(s_x, \xi_x)}{\partial {s_x}^2} + i \cdot \frac{\partial \boldsymbol{\Phi}_x(s_x, \xi_x)}{\partial \xi_x} = 0 \\ \frac{1}{2} \cdot \frac{\partial^2 \boldsymbol{\Phi}_y(s_y, \xi_y)}{\partial {s_y}^2} + i \cdot \frac{\partial \boldsymbol{\Phi}_y(s_y, \xi_y)}{\partial \xi_y} = 0 \end{aligned} \tag{42}$$

Physical solutions to Equations (42) are:

$$\begin{aligned} \Phi_x(s_x, \xi_x; a_x) &= \mathbb{Ai}\left[(s_x + a_x) - \left(\frac{\xi_x}{2}\right)^2\right] \cdot e^{i \cdot \left[\left(-\frac{\xi_x^3}{12}\right) + (s_x + a_x) \cdot \frac{\xi_x}{2}\right]} \\ \Phi_y(s_y, \xi_y; a_y) &= \mathbb{Ai}\left[(s_y + a_y) - \left(\frac{\xi_y}{2}\right)^2\right] \cdot e^{i \cdot \left[\left(-\frac{\xi_y^3}{12}\right) + (s_y + a_y) \cdot \frac{\xi_y}{2}\right]} \end{aligned} \tag{43}$$

where $\mathbb{Ai}(\cdot)$ is an Airy function (one function of the pair of Airy functions solving $w'' - zw = 0$, Abramowitz and Stegun (1964), equation 10.4.1).

The Airy Infinite Beams solution $[\psi^{AiI}(x, y, z; a_x, a_y)]$ to the SVEA-PWE (Equation 5) is thus:

$$\mathcal{F}^{AiI}(x, y, z; a_x, a_y) = \Phi_x[S_x(x), \xi_x(z);\ a_x] \cdot \Phi_y[s_y(y), \xi_y(z); a_y]$$
$$\psi^{AiI}(x, y, z; a_x, a_y) = \mathcal{F}^{AiI}(x, y, z; a_x, a_y) \cdot e^{i \cdot k_H \cdot z}. \tag{44}$$

Note that for Airy Infinite Beams (as well as for other types of Airy Beams), the accumulation of phase of the electric field, along (for example) the axial axis ($x = 0, y = 0$) is not a straight line ($k_z \cdot z$), but rather, a third-order polynomial:

$$Phase_{Airy}(0, 0, z; a_x, a_y, k_H) = -\frac{[\xi_x(z)]^3}{12} + a_x \cdot \frac{\xi_x(z)}{2} - \frac{[\xi_y(z)]^3}{12} + a_y \cdot \frac{\xi_y(z)}{2} + k_H \cdot z \tag{45}$$

Curves of accumulated phase along the axial axis for a Plane Infinite Beam and for an Airy Infinite Beam are shown in Figure 8.

Examples of (accelerating/nondiffracting) intensity patterns of an Airy Infinite Beam (44) are shown in Figure 9.

3.1.3 Airy Finite Beams

Airy Infinite Beams (Equation 44) extend to infinity in the transverse plane and carry an infinite amount of energy. However, Siviloglou and Christodoulides (2007), based on the translation invariance properties of the SVEA-PWE (Equation 5), presented a finite-energy solution:

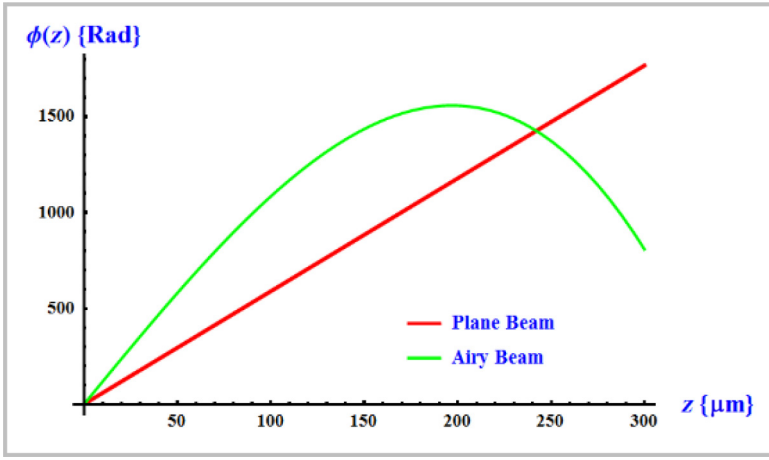

Figure 8 Phase accumulation along the axial axis for a Plane Infinite Beam (red (dark gray in the print version)) and for an Airy Infinite Beam (green (gray in the print version)) (Equation 45).

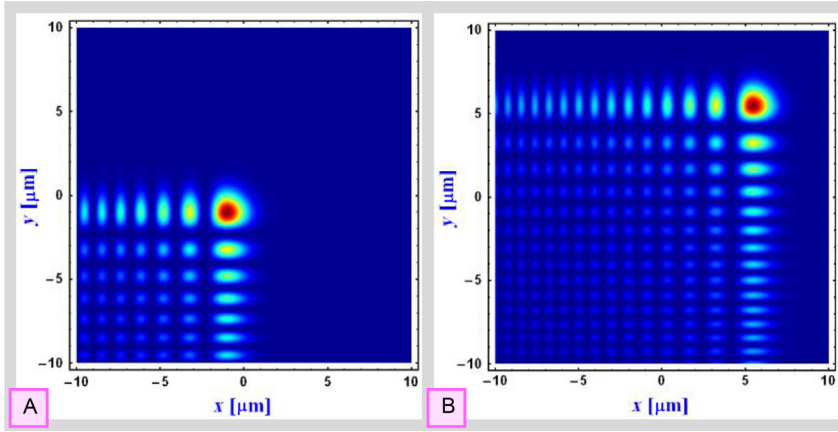

Figure 9 Intensity patterns due to an Airy Infinite Beam. (A) $z = 0$. (B) $z = 60\mu m$. The patterns accelerate (yet do not diffract—cf. Table 3).

$$\Phi_x(s_x, \xi_x; \nu_x, a_x) = \mathbb{Ai}\left[s_x - \left(\frac{\xi_x}{2}\right)^2 - \nu_x \cdot \xi_x + i \cdot a_x \cdot \xi_x\right] \cdot e^{\left[a_x \cdot s_x - \left(\frac{a_x \cdot \xi_x^2}{2}\right) - a_x \cdot \nu_x \cdot \xi_x\right]} \cdot e^{i \cdot \left[\left(-\frac{\xi_x^3}{12}\right) + (a_x^2 - \nu_x^2 + s_x) \cdot \frac{\xi_x}{2} + \nu_x \cdot s_x - \left(\frac{\nu_x \cdot \xi_x^2}{2}\right)\right]} \quad (46)$$

$$Re[a_x] > 0\,; \quad \text{Slow diffraction if } Re[a_x] \ll 1$$

and similarly for $\Phi_y(s_y, \xi_y; \nu_y, a_y)$ with $x \longrightarrow y$.

The Airy Finite Beams solution $[\psi^{AiF}(x, y, z; \nu_x, a_x, \nu_y, a_y)]$ to the SVEA-PWE (Equation 5) is thus

$$\mathcal{F}^{AiF}(x, y, z; \nu_x, a_x, \nu_y, a_y) = \Phi_x[S_x(x), \xi_x(z); \nu_x, a_x] \cdot \Phi_y[S_y(y), \xi_y(z); \nu_y, a_x]$$
$$\psi^{AiF}(x, y, z; \nu_x, a_x, \nu_y, a_y) \equiv \mathcal{F}^{AiF}(x, y, z; \nu_x, a_x, \nu_y, a_y) \cdot e^{i \cdot k_H \cdot z} \quad (47)$$

Note that now the argument of the Airy function ($\mathbb{Ai}(\cdot)$ in 46) includes a z-dependent complex component ($i \cdot a_x \cdot \xi_x$) and so the pattern not only translates but gradually changes (diffracts). The rate of diffraction depends, of course, on the value of the *decay factor* (a_x) (Siviloglou & Christodoulides, 2007).

Examples of (accelerating/slowly diffracting) intensity patterns of an Airy Finite Beam (47) are shown in Figure 10.

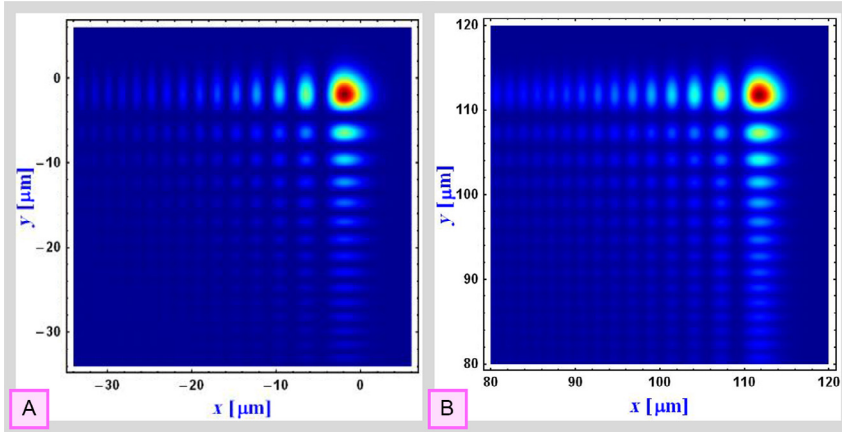

Figure 10 Intensity patterns due to an Airy Finite Beam. (A) $z = 0$. (B) $z = 200\mu m$ (decay factor = 0.05). The patterns accelerate and slowly diffract (cf. Table 3. Other parameters such as wavelength—cf. Equation 16). Looking at the (B) pattern, note the slight change in intensity distribution at the top-right corner and the slight wash out of the pattern (vs. the (A) pattern). Compare this figure patterns with the patterns in Figure 9 to see the introduced left and down decay.

3.1.4 Airy–Airy Beams

In a paper by Bandres (2009), a new family of (an infinite energy) accelerating beams was suggested. Two sister beams of that new family, having a closed-form mathematical expression (along with parabolic beams as discussed in Section 3.3.1), are Airy-related. Here, we name these two beam-sets—*Airy–Airy Beams* and *Airy–Plane Beams*.

The Airy–Airy Beams solution $[\psi^{AAB}(x, y, z; \lambda, \beta)]$ to the SVEA-PWE (Equation 5) is given as:

$$\mathcal{F}^{AAB}(x, y, z; \lambda, \beta) = Ai\left(\frac{u - \lambda - \zeta^2 - v + \beta}{2^{\frac{2}{3}}}\right) * Ai\left(\frac{u - \lambda - \zeta^2 + v - \beta}{2^{\frac{2}{3}}}\right)$$
$$\psi^{AAB}(x, y, z; \lambda, \beta) = \mathcal{F}^{AAB}(x, y, z; \lambda, \beta) \cdot e^{i \cdot k_H \cdot z}$$
$$u \equiv \frac{x}{\kappa};\ v \equiv \frac{x}{\kappa};\ \zeta \equiv \frac{z}{2 \cdot k_H \cdot \kappa^2};\ \lambda \in \mathbb{R};\ \beta \in \mathbb{R} \tag{48}$$

Examples of (accelerating/nondiffracting) intensity patterns of an Airy–Airy Beam (48) are shown in Figure 11.

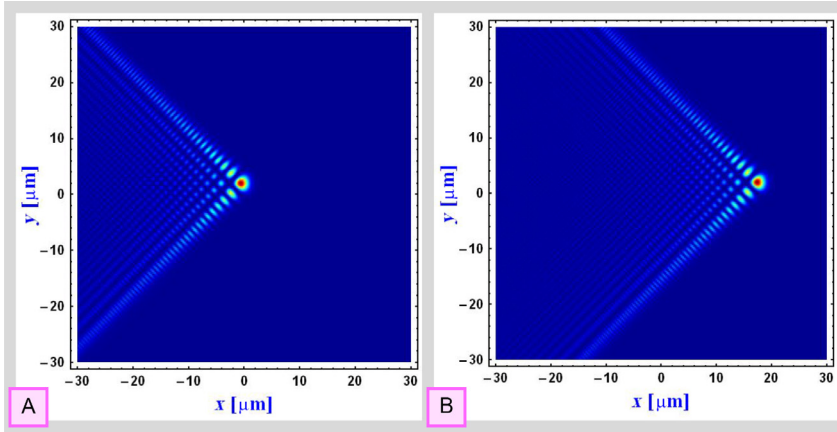

Figure 11 Intensity patterns due to an Airy–Airy Beam. (A) $z = 0$. (B) $z = 1000\,\mu m$. The patterns accelerate but otherwise remain unchanged.

3.1.5 Airy–Plane Beams

The second sister beam-set described in the above cited paper (Bandres, 2009) is the set we name here Airy–Plane Beams. A later paper by Ruelas, Davis, Moreno, Cottrell, and Bandres (2014) presented a recipe for the construction of *accelerating light beams with arbitrarily transverse shapes* with Airy–Plane Beams as the basis functions.

The Airy–Plane Beams solution $[\psi^{APB}(x, y, z; \lambda, \Omega)]$ to the SVEA-PWE (Equation 5) is given as:

$$\begin{aligned} &\mathcal{F}^{APB}(x, y, z; \lambda, \Omega) = Ai\left(u - \lambda - \zeta^2 + \Omega^2\right) \\ &* \exp\left[i \cdot \zeta \cdot \left(u - \lambda - \zeta^2\right) + i \cdot \frac{\zeta^3}{3} + i \cdot \Omega \cdot v\right] \\ &\psi^{APB}(x, y, z; \lambda, \Omega) = \mathcal{F}^{APB}(x, y, z; \lambda, \Omega) \cdot e^{i \cdot k_H \cdot z} \\ &u \equiv \frac{x}{\kappa};\ v \equiv \frac{x}{\kappa};\ \zeta \equiv \frac{z}{2 \cdot k_H \cdot \kappa^2};\ \lambda \in \mathbb{R};\ \Omega \in \mathbb{R} \end{aligned} \tag{49}$$

Examples of (accelerating/nondiffracting) intensity patterns of an Airy–Plane Beam (49) are shown in Figure 12.

3.1.6 Hermite–Gauss Beams

Another well-known solution to each of Equations (36) is the Hermite–Gauss function (Siegman, 1973, 1986), written here in one transverse dimension:

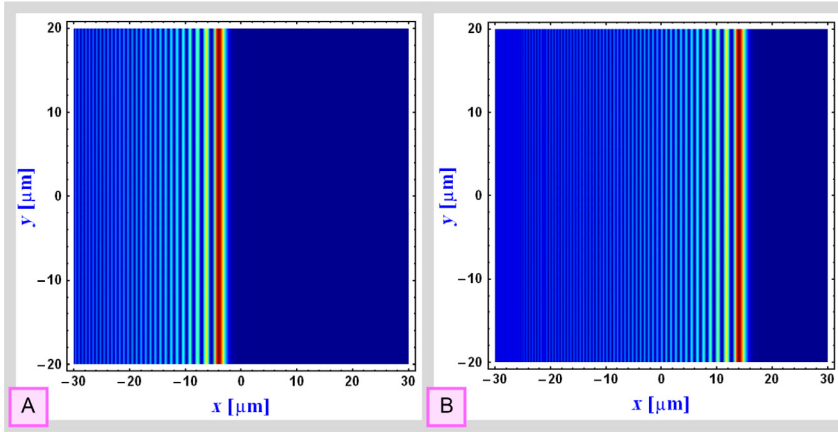

Figure 12 Intensity patterns due to an Airy–Plane Beam. (A) $z = 0$. (B) $z = 1000\,\mu m$. The patterns accelerate but otherwise remain unchanged.

$$\begin{gathered}\Phi_x(x,z;m) = A^m_{H-G}\cdot\left[\frac{\sigma(0)}{\sigma(z)}\right]^{\frac{1}{2}}\cdot H_m\left(\frac{x}{\sigma(z)}\right)\cdot\exp\left(-\frac{x^2}{2\cdot\sigma(z)^2}\right)\cdot \\ \exp\left[i\cdot\left(\frac{k_H\cdot x^2}{2\cdot R(z)}-(m+0.5)\cdot\psi_G(z)\right)\right] \\ \sigma(z)\equiv\frac{\omega(z)}{2};\ \omega(z)\equiv\omega_0\cdot\sqrt{1+z_N^2};\ R(z)\equiv z\cdot\left[1+\left(\frac{1}{z_N}\right)^2\right] \\ Z_N\equiv\frac{z}{z_R};\ Z_R\equiv\frac{1}{2}\cdot k_H\cdot\omega_0^2;\ \psi_G(Z)\equiv\operatorname{atan}(Z_N)\end{gathered} \tag{50}$$

And similarly for $\Phi_y(y,z;n)$ with $x\longrightarrow y$ and $m\longrightarrow n$. In Equation (50)—A^m_{H-G} are normalizing amplitudes (for Hermite–Gaussian functions), and $H_m\left(\frac{x}{\sigma(z)}\right)$ is a Hermite Polynomial of order m (Arfken et al., 2012, chapter 18).

The Hermite–Gauss Beams solution $[\psi^{HGB}(x,y,z;m,n)]$ to the SVEA-PWE (Equation 5) is thus:

$$\begin{gathered}\mathcal{F}^{HGB}(x,y,z;m,n) = \Phi_x(x,z;m)\cdot\Phi_y(y,z;n) \\ \psi^{HGB}(x,y,z;m,n)\equiv\mathcal{F}^{HGB}(x,y,z;m,n)\cdot e^{i\cdot k_H\cdot z}\end{gathered} \tag{51}$$

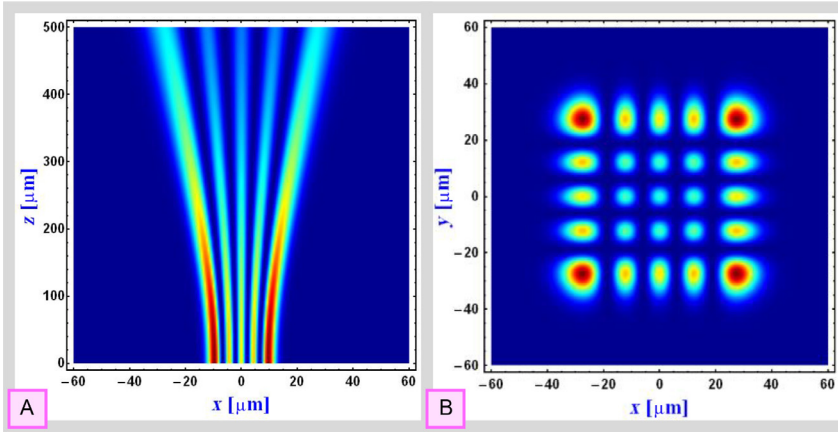

Figure 13 Intensity patterns due to a centered Hermite–Gauss Beam. (A) $(x,0,z)$ plane. (B) $(x,y,0)$ plane. The patterns expand but otherwise remain unchanged.

In fact, a more general solution to the SVEA-PWE (Equation 5) is a *Decentered Hermite–Gauss* solution which is Equation (51) with $(x, y) \longrightarrow (x - x_d, y - y_d)$, based on the translation invariance of Equations (38), in addition to a *tilt* (Schimpf, Schulte, Putnam, & Kärtner, 2012).

Examples of (expanding) intensity patterns of a *centered* Hermite–Gauss beam (51) are shown in Figure 13.

3.1.7 Plane–Gauss Beams

Following Gutiérrez-Vega and Bandres (2005), the Plane–Gauss Beams solution $[\psi^{PGB}(x, y, z; k_x, k_y)]$ to the SVEA-PWE (Equation 5) is given by:

$$\psi^{PGB}(x, y, z; k_x, k_y) = e^{-i \cdot \frac{k_t^2}{2 \cdot k_H} \cdot \frac{z}{\mu}} \cdot GB(x, y, z) \cdot \left(A_x \cdot e^{i \cdot k_x \cdot \frac{x}{\mu}} + B_x \cdot e^{-i \cdot k_x \cdot \frac{x}{\mu}}\right) \cdot \left(A_y \cdot e^{i \cdot k_y \cdot \frac{y}{\mu}} + B_y \cdot e^{-i \cdot k_y \cdot \frac{y}{\mu}}\right) \quad (52)$$

Examples of (diffracting) intensity patterns of a Plane–Gauss Beam (52) are shown in Figure 14. The shown starting pattern (A) is a superposition of seven plane waves (cf. Figure 7 in Section 3.1.1), this time under a limiting Gaussian. The patterns in general carry a finite amount of energy. The

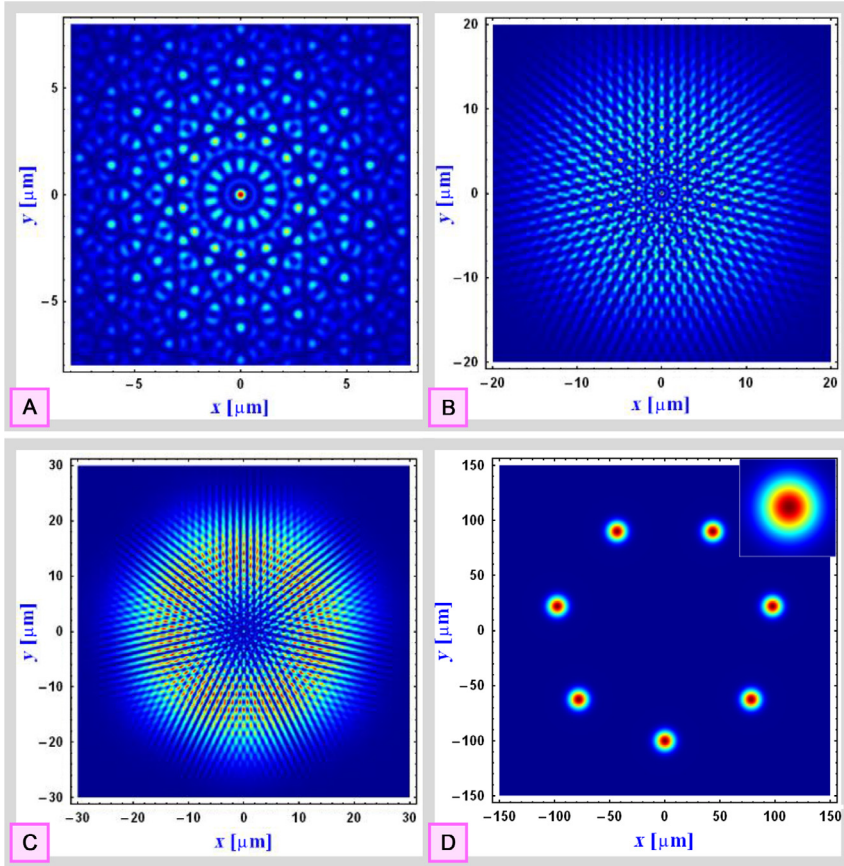

Figure 14 Intensity patterns due to Plane–Gauss Beams at four axial distances $[z(A,B,C,D) = (0, 20, 30, 200)\,\mu\text{m}]$. The initial (finite energy) pattern is a superposition of seven plane waves (cf. Figure 7 in Section 3.1.1), this time under a limiting Gaussian (Equation 52). The pattern propagates in a fast-expansion mode $[\omega_0 > 2/k_t]$ (cf. Section 1.6 and see Figure 2). The inset in (D) is just a zoom-in to one of the seven diffraction spots visible under the (formed) Gaussian ring. Clearly the pattern diffracts (cf. Table 3).

shown pattern is propagating in a fast-expansion mode $[\omega_0 > 2/k_t]$ (cf. Section 1.6 and see Figure 2). The inset in (D) is just a zoom-in to one of the seven diffraction spots visible under the (formed) Gaussian ring. Clearly the pattern diffracts (cf. Table 3).

3.2 Circular–Cylindrical coordinates

In circular–cylindrical coordinates (cf. Equation 17), The SVEA-PWE (Equation 5) is transformed to

$$\frac{1}{\rho^2}\cdot\frac{\partial^2\mathcal{F}(\rho,\varphi,z)}{\partial\varphi^2}+\frac{1}{\rho}\cdot\frac{\partial}{\partial\rho}\left[\rho\cdot\frac{\partial\mathcal{F}(\rho,\varphi,z)}{\partial\rho}\right]+i\cdot 2\cdot k_H\cdot\frac{\partial\mathcal{F}(\rho,\varphi,z)}{\partial z}=0 \tag{53}$$

with a well-known solution in terms of Laguerre–Gauss beams which we will now consider.

3.2.1 Laguerre–Gauss Beams

The SVEA-PWE in circular–cylindrical coordinates (Equation 53) is solved by the well-known Laguerre–Gauss functions (Carbone, Bogan, Fulda, Freise, & Willke, 2013; Siegman, 1986). Thus, the solutions to the SVEA-PWE (Equation 5) in circular–cylindrical coordinates $[\psi^{LGB}(\rho,\varphi,z;p,l)]$ are Laguerre–Gauss Beams:

$$\begin{aligned}\mathcal{F}^{LGB}(\rho,\varphi,z;p,l)&=\left[\frac{2\cdot p!}{\pi\cdot(|l|+p)!}\right]^{\frac{1}{2}}\cdot\frac{1}{\omega(z)}\cdot e^{i\cdot(2\cdot p+|l|+1)\cdot\psi_G(z)}\cdot\left[\frac{\sqrt{2}\cdot\rho}{\omega(z)}\right]^{|l|}\cdot\\&\quad L_p^{|l|}\left(\frac{2\cdot\rho^2}{[\omega(z)]^2}\right)\cdot e^{-i\cdot k_H\cdot\frac{\rho^2}{2\cdot q(z)}+i\cdot l\cdot\varphi}\\q(z)&\equiv z+i\cdot z_R\\p&=0,1,2,\ldots,;\ l=\ldots,-2,-1,0,1,2,\ldots\\\psi^{LGB}(\rho,\varphi,z;p,l)&=\mathcal{F}^{LGB}(\rho,\varphi,z;p,l)\cdot e^{i\cdot k_H\cdot z}\end{aligned} \tag{54}$$

In Equation (54), $L_p^{|l|}$ are the generalized Laguerre polynomials (Abramowitz & Stegun, 1964), and the functions $\omega(z)$, are defined by Equation (50).

Examples of (expanding) intensity patterns of a Laguerre–Gauss Beam (54) are shown in Figure 15. The patterns in the top row of the figure show the intensity of only the real part of the beam $\{|Re(\psi^{LGB}(\rho,\varphi,z;p,l))|^2\}$.

3.2.2 Bessel–Gauss Beams

The Bessel–Gauss Beams solution $[\psi^{BGB}(\rho,\varphi,z;k_t,l)]$ to the SVEA-PWE (Equation 5), is given as (Gutiérrez-Vega & Bandres, 2005, see Equation (20) for the generating Bessel Wave):

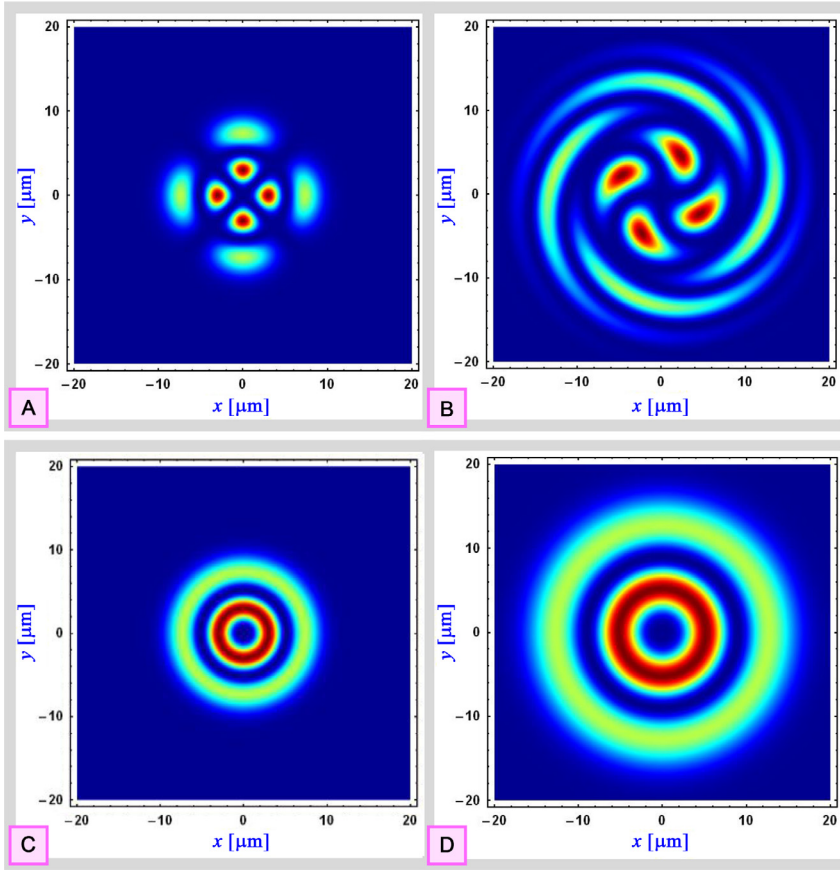

Figure 15 Intensity patterns due to a Laguerre–Gauss Beam (Equation 54). (A and B) $|\mathrm{Re}(\psi^{LGB}(\rho,\varphi,z;p,l))|^2$. (C and D) $|(\psi^{LGB}(\rho,\varphi,z;p,l))|^2$. (A and C) $z=0$. (C and D) $z=150\,\mu\mathrm{m}$. The Intensity patterns (C and D) expand but otherwise remain unchanged.

$$\psi^{BGB}(\rho,\varphi,z;k_t,l) = e^{-i\cdot\frac{k_t^2}{2\cdot k_H}\cdot\frac{z}{\mu}}\cdot GB(\rho,z)\cdot J_l\left(\frac{k_t\cdot\rho}{\mu}\right)\cdot \left(A_l\cdot e^{i\cdot l\cdot\varphi}+B_l\cdot e^{-i\cdot l\cdot\varphi}\right) \tag{55}$$

Bessel–Gauss Beams (with focus on the zero-order Bessel function) and their diffraction characteristics were first considered by Gori et al. (1987). Here, we extended these derived diffraction characteristics to apply to all four wave-originated beams, one of which is the Bessel–Gauss Beam (Gutiérrez-Vega & Bandres, 2005, cf. Section 1.2.2). A few years ago, a novel class of higher order Bessel–Gauss beams defined as superpositions of decentered Hermite–Gaussian beams was reported (Schimpf et al., 2012).

Examples of (diffracting) intensity patterns of a Bessel–Gauss Beam (55) are shown in Figure 16. The shown starting pattern (a) is a Bessel Wave (cf. Figure 4 in Section 3.1.1), this time under a limiting Gaussian. The patterns in general carry a finite amount of energy. The shown pattern is propagating in a fast-expansion mode [$\omega_0 > 2/k_t$] (cf. Section 1.6 and see Figure 2). The spots in (e) are visible under the (formed) Gaussian ring (f). Clearly the pattern diffracts (cf. Table 3).

3.3 Parabolic–Cylindrical coordinates

Discussed next are three sets of beams that solve the SVEA-PWE (Equation 5) in the parabolic–cylindrical coordinate system.

3.3.1 Parabolic Infinite Beams

To solve the SVEA-PWE (Equation 5) in parabolic–cylindrical coordinates (Equation 21), let's first define dimensionless variables (Bandres, 2008):

$$u \equiv \frac{x}{\kappa};\ v \equiv \frac{y}{\kappa};\ \zeta \equiv \frac{z}{2 \cdot k_H \cdot \kappa^2} \tag{56}$$

and write the SVEA-PWE (Equation 5) in these Cartesian dimensionless coordinates:

$$\frac{\partial^2 \mathcal{F}(u,v,\zeta)}{\partial u^2} + \frac{\partial^2 \mathcal{F}(u,v,\zeta)}{\partial v^2} + i \cdot \frac{\partial \mathcal{F}(u,v,\zeta)}{\partial \zeta} = 0 \tag{57}$$

In parabolic coordinates (Bandres, 2008, cf. Equations 21 and 56):

$$\left(u - \lambda - \zeta^2, v\right) = \left(\frac{\eta^2}{2} - \frac{\xi^2}{2}, \eta\xi\right), \tag{58}$$

the solution to Equation (57) is given as

$$\mathcal{F}^{PaI}(u,v,\zeta;\lambda,n) = e^{i \cdot \mathbf{\Phi}^{PaI}(\eta,\xi,\zeta)} \cdot \boldsymbol{\theta}_n(\eta) \cdot \boldsymbol{\theta}_n(i \cdot \xi);\ n = 0,1,2,\ldots \tag{59}$$

with

$$\mathbf{\Phi}^{PaI}(\eta,\xi,\zeta) \equiv \zeta \cdot \frac{\left(\eta^2 - \xi^2\right)}{2} + \frac{\zeta^3}{3} \tag{60}$$

and $\boldsymbol{\theta}_n(\eta), \boldsymbol{\theta}_n(i \cdot \xi)$ are, respectively, the solutions to the *quartic potential Schrödinger equation* (Banergee, Bhatnagar, Choudhry, & Kanwal, 1978; Dusuel & Uhrig, 2004) with the Hamiltonian $H = \frac{p^2}{2} + \frac{x^4}{4}$ and to its *modified* (or *associated*) version (for the nth eigenvalue):

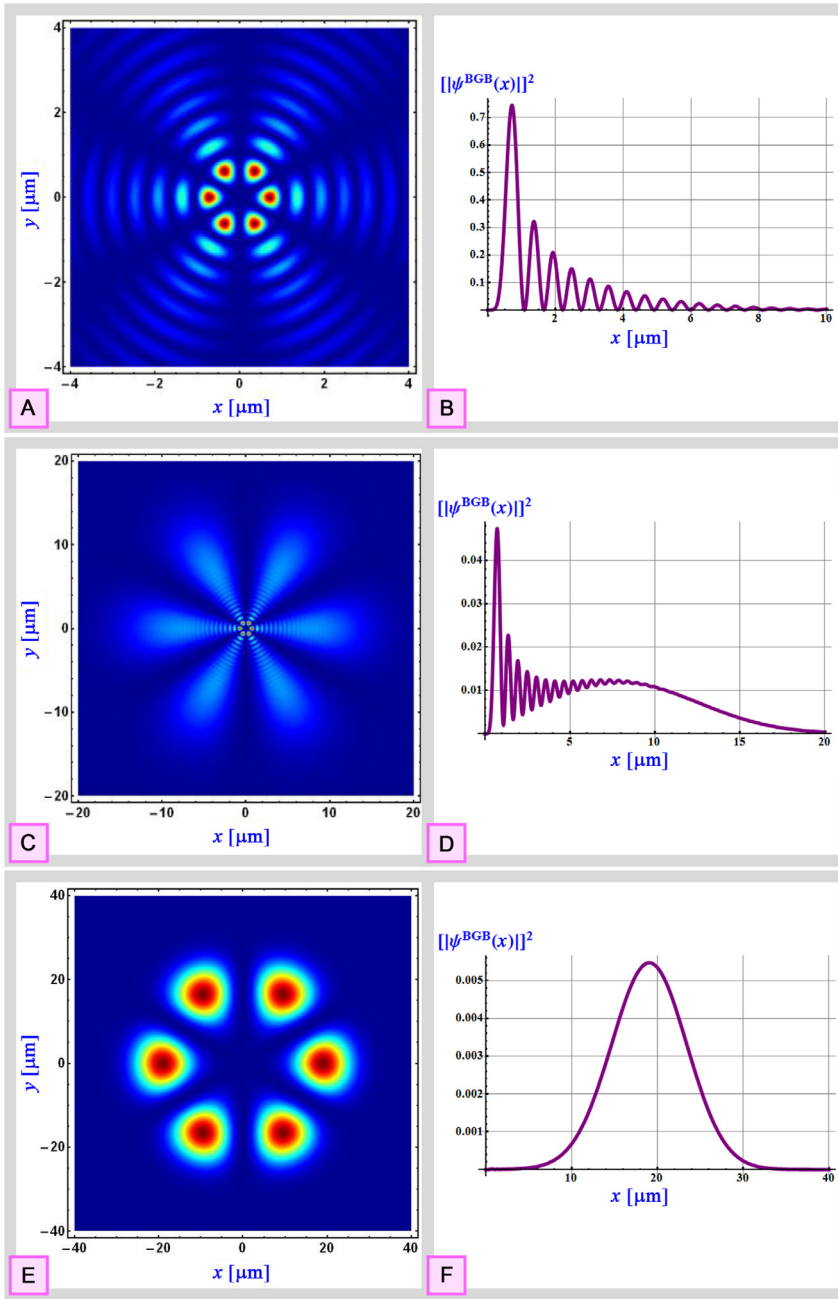

Figure 16 Intensity patterns due to a Bessel–Gauss Beam (Equation 55). The shown pattern is propagating in a fast-expansion mode $[\omega_0 > 2/k_t]$ (cf. Section 1.6 and see Figure 2). The curves in (b, d, and f) are intensity cross sections along the x-axis $\{|\psi^{BGB}(x,0,z_i)|^2\}$ at $z_i = (0, 20, 40)\mu$m (cf. figure 1 of Gori et al., 1987).

$$\left(-\frac{\partial_{\eta\eta}}{2}+\frac{\eta^4}{4}\right)\mathbb{N}(\eta)=E\cdot\mathbb{N}(\eta)$$
$$\left(\frac{\partial_{\xi\xi}}{2}+\frac{\xi^4}{4}\right)\mathbb{X}(\xi)=E\cdot\mathbb{X}(\xi) \tag{61}$$

The Parabolic Infinite Beam solution $[\psi^{PaI}(u,v,\zeta;\lambda,n)]$ to the SVEA-PWE (Equation 5) is thus:

$$\psi^{PaI}(u,v,\zeta;\lambda,n)=\mathcal{F}^{PaI}(u,v,\zeta;\lambda,n)\cdot e^{i\cdot k_H\cdot z} \tag{62}$$

Examples of (accelerating) intensity patterns of two high order Parabolic Infinite Beams (62) are shown in Figure 17.

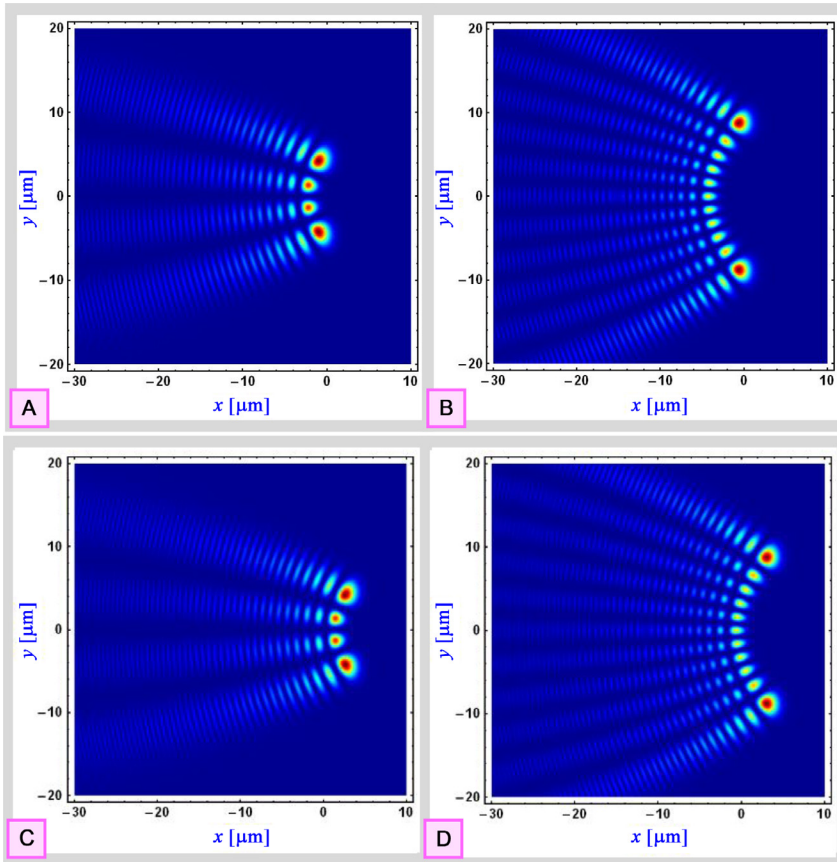

Figure 17 Intensity patterns due to two high order Parabolic Infinite Beams (Equation 62). (a and b) $z=0$. (c and d) $z=45\,\mu$m. The intensity patterns accelerate but otherwise remain unchanged.

3.3.2 Parabolic Finite Beams

Based on the translation invariance of the SVEA-PWE (Equation 5), the expression for finite-energy parabolic beams is derived (Bandres, 2008) as:

$$\begin{gathered}\mathcal{F}^{PaF}(u,v,\zeta;\lambda,n,a)=e^{i\cdot\boldsymbol{\Phi}^{PaF}(\eta,\xi,\zeta,a)}\cdot\boldsymbol{\theta}_n(\eta)\cdot\boldsymbol{\theta}_n(i\cdot\xi);n=0,1,2,\ldots\\ \left(u-\left(\lambda+a^2\right)-(\zeta-i\cdot a)^2,v\right)=\left(\frac{\eta^2}{2}-\frac{\xi^2}{2},\eta\xi\right)\\ \boldsymbol{\Phi}^{PaF}(\eta,\xi,\zeta,a)\equiv(\zeta-i\cdot a)\cdot\frac{\left(\eta^2-\xi^2\right)}{2}+\frac{(\zeta-i\cdot a)^3}{3}\\ Re[a]>0;\ \textit{Slow diffraction if } Re[a]\ll 1\end{gathered}\tag{63}$$

with $[\boldsymbol{\theta}_n(\eta),\boldsymbol{\theta}_n(i\cdot\xi)]$ as defined above (Equation 61).

The Parabolic Finite Beam solution $[\psi^{PaF}(u,v,\zeta;\lambda,n,a)]$ to the SVEA-PWE (Equation 5) is thus:

$$\psi^{PaF}(u,v,\zeta;\lambda,n,a)=\mathcal{F}^{PaF}(u,v,\zeta;\lambda,n,a)\cdot e^{i\cdot k_H\cdot z}\tag{64}$$

Note that now, with the introduction of a *decay factor* (a), the arguments (η,ξ) of the functions $[\boldsymbol{\theta}_n(\eta),\boldsymbol{\theta}_n(i\cdot\xi)]$ solving Equations (61) are complex. This is why patterns of Parabolic Finite Beams diffract (Bandres, 2008). The diffraction rate depends on the value of the decay factor. Recall the very similar diffraction characteristics of Airy Finite Beams (Section 3.1.3 and Figure 10).

Examples of (accelerating and slowly diffracting) intensity patterns of a high order Parabolic Finite Beam (64) are given in Figure 18.

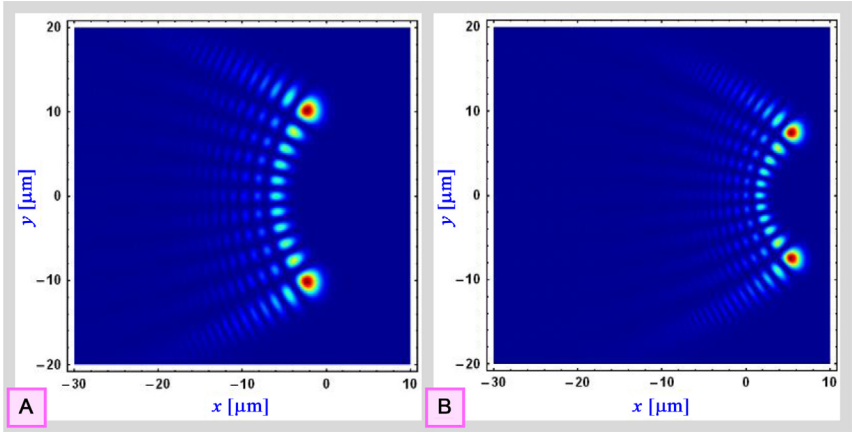

Figure 18 Intensity patterns due to a high order Parabolic Finite Beam (Equation 64). (a) $z=0$. (b) $z=50\,\mu$m. The intensity patterns accelerate and slowly diffract. The patterns' decay going to negative x values is due to the introduced decay factor (a) (compare with the patterns for the Parabolic Infinite Beams—Figure 17).

3.3.3 Weber–Gauss Beams

The Weber–Gauss Beams solution $[\psi^{WGB}(\eta, \xi, z; a, k_t)]$ to the SVEA-PWE (Equation 5) is given as (Gutiérrez-Vega & Bandres, 2005, see also *parabolic-Gauss* beams in Forbes, 2014, chapter 8):

$$\begin{aligned}\psi^{WGB}(\eta, \xi, z; a, k_t) = \; & e^{-i \cdot \frac{k_t^2}{2 \cdot k_H} \cdot \frac{z}{\mu}} \cdot GB(x, y, z) \cdot \\ & \psi^{WBR}\left[\eta\left(\frac{x}{\mu}, \frac{y}{\mu}\right), \xi\left(\frac{x}{\mu}, \frac{y}{\mu}\right); a, k_t\right]\end{aligned} \tag{65}$$

where $\psi^{WBR}(\eta, \xi; a, k_t)$ is the transverse part of the Weber Wave pattern given by Equation (24).

Examples of (diffracting) intensity patterns of a Weber–Gauss Beam (55) are shown in Figure 19. The shown starting patterns (a and b) are even and odd Weber Waves (cf. Figure 5 in Section 2.4), this time under a limiting Gaussian. The patterns in general carry a finite amount of energy. The shown patterns are propagating in a fast-expansion mode $[\omega_0 > 2/\mathrm{k_t}]$ (cf. Section 1.6 and see Figure 2). The spots in E and in F are visible under the (formed) Gaussian ring. Clearly the patterns diffract (cf. Table 3).

3.4 Elliptical–Cylindrical coordinates

The last two sets of beams reviewed here solve the SVEA-PWE (Equation 5) in an elliptical–cylindrical coordinate system.

3.4.1 Ince–Gauss Beams

The SVEA-PWE (Equation 5) in z-dependent elliptical–cylindrical coordinates:

$$\begin{gathered}x = f(z) \cdot \cosh(\xi) \cos(\eta); y = f(z) \cdot \sinh(\xi) \sin(\eta); z = z \\ f(z) \equiv \frac{\mathrm{f}_0 \cdot \omega(z)}{\omega_0}\end{gathered} \tag{66}$$

is solved by Ince–Gauss functions (Bandres & Gutiérrez-Vega, 2004a):

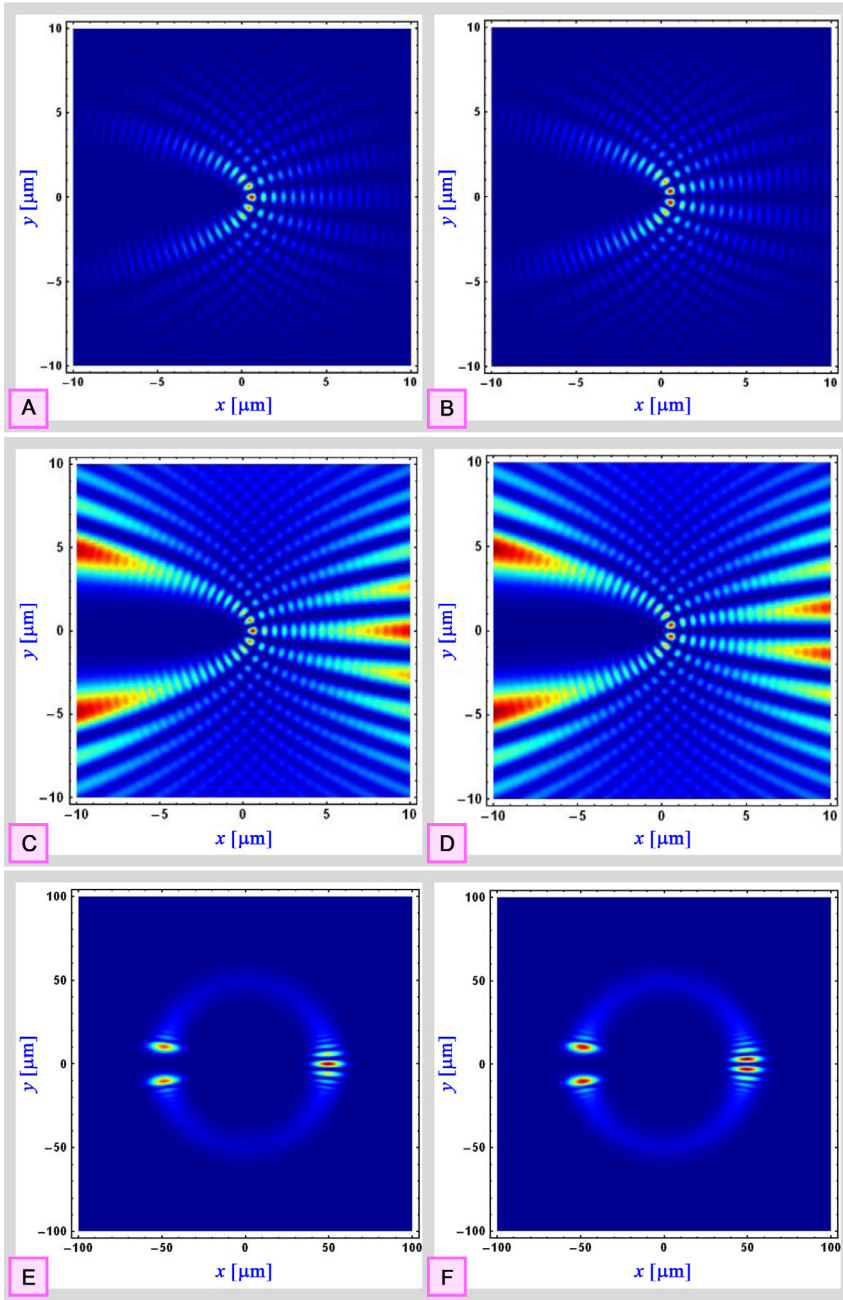

Figure 19 Intensity patterns due to Weber–Gauss Beams (Equation 65). Left: even. Right: odd. Top: $z = 0$. Center: $z = 30\,\mu m$. Bottom: $z = 100\,\mu m$. The shown patterns propagate in a fast-expansion mode [$\omega_0 > 2/k_t$] (cf. Section 1.6 and see Figure 2). Clearly the patterns diffract.

$$
\begin{aligned}
\psi_e^{IGB}(x,y,z;p,m,\varepsilon) &= \frac{C\cdot\omega_0}{\omega(z)}\cdot C_p^m(i\cdot\xi;\varepsilon)\cdot \\
&\quad C_p^m(\eta;\varepsilon)\cdot e^{-\frac{x^2+y^2}{\omega^2(z)}}\cdot \exp \\
&\quad \left[i\cdot\left(\frac{k_H\cdot(x^2+y^2)}{2\cdot R(z)}-(p+1)\cdot\psi_G(z)\right)\right]\cdot e^{i\cdot k_H\cdot z} \\
&\quad 0\le m\le p;(-1)^{p-m}=1 \\
\psi_0{}^{IGB}(x,y,z;p,m,\varepsilon) &= \frac{S\cdot\omega_0}{\omega(z)}\cdot S_p^m(i\cdot\xi;\varepsilon)\cdot \\
&\quad S_p^m(\eta;\varepsilon)\cdot e^{-\frac{x^2+y^2}{\omega^2(z)}}\cdot \exp \\
&\quad \left[i\cdot\left(\frac{k_H\cdot(x^2+y^2)}{2\cdot R(z)}-(p-1)\cdot\psi_G(z)\right)\right]\cdot e^{i\cdot k_H\cdot z} \\
&\quad 1\le m\le p;(1-)^{p-m}=1
\end{aligned}
\tag{67}
$$

The functions $\omega(z)$, $R(z)$ and $\psi_G(z)$ are as those already defined by Equation (50). The functions $C_p^m(\eta;\epsilon)$ and $S_p^m(\eta;\epsilon)$ are, respectively, the even and odd Ince Polynomials solving the Ince equation (Arscott, 1967) (top of Equation 68) and the functions $C_p^m(i\cdot\xi;\epsilon)$ and $S_p^m(i\cdot\xi;\epsilon)$ are, respectively, the even and odd Ince Polynomials with a complex argument solving the *modified* Ince equation (bottom of Equation 68):

$$
\begin{aligned}
&\frac{d^2\mathbb{N}(\eta)}{d\eta^2}-\varepsilon\cdot\sin(2\cdot\eta)\cdot\frac{d\mathbb{N}(\eta)}{d\eta}+[a-p\cdot\varepsilon\cdot\cos(2\cdot\eta)]\cdot\mathbb{N}(\eta)=0 \\
&\frac{d^2\mathbb{E}(\xi)}{d\xi^2}-\varepsilon\cdot\sinh(2\cdot\xi)\cdot\frac{d\mathbb{E}(\xi)}{d\xi}-[a-p\cdot\varepsilon\cdot\cosh(2\cdot\xi)]\cdot\mathbb{E}(\xi)=0 \\
&\varepsilon\equiv\frac{2\cdot f_0^2}{\omega_0^2}
\end{aligned}
\tag{68}
$$

Note: The parameter a in Equation (68) was chosen such that the physical solutions (67) (Bandres & Gutiérrez-Vega, 2004a, 2004b) are *trigonometric polynomials*, *called Ince polynomials* of a defined parity and therefore does not explicitly appear in the SVEA-PWE solutions (Equation 67). An extensive numerical and experimental work on laser selective-excitation of Ince–Gauss Beams was performed by Chu and Otsuka (2007) and Ohtomo, Chu, and Otsuka (2008). A Matlab package for calculating

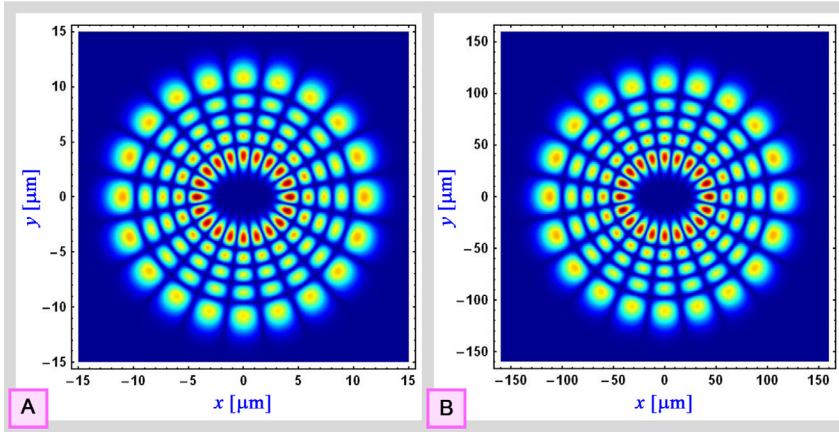

Figure 20 Intensity patterns due to a high order Ince–Gauss Beam (Equation 67). (a) $z = 0$. (b) $z = 480\,\mu m$. The patterns expand but otherwise remain unchanged.

Ince–Gaussian beams at a given z-plane was provided by M.A. Bandres and is available via an internet link (Bandres, 2014).

Examples of (expanding) intensity patterns of an Ince–Gauss Beam (67) are provided in Figure 20.

3.4.2 Mathieu–Gauss Beams

General Mathieu waves (Equation 33), can be split into even and odd Mathieu waves:

$$\begin{aligned}\psi_e^{MTH}(\zeta,\phi,z;\lambda_{t,n},Q_t) &= A_e\cdot ce_n(\phi;Q_t)\cdot Je_n(\zeta;Q_t)\cdot e^{i\cdot k_z\cdot z}\\ \psi_o^{MTH}(\zeta,\phi,z;\lambda_{t,n},Q_t) &= A_o\cdot se_n(\phi;Q_t)\cdot Jo_n(\zeta;Q_t)\cdot e^{i\cdot k_z\cdot z}\end{aligned} \tag{69}$$

The even $[\psi_e^{MGB}(x,y,z;\lambda_{t,n},Q_t)]$ and odd $[\psi_o^{MGB}(x,y,z;\lambda_{t,n},Q_t)]$ Mathieu–Gauss Beams solutions to the SVEA-PWE (Equation 5) in elliptical–cylindrical coordinates (Equation 25) are given by (Gutiérrez-Vega & Bandres, 2005):

$$\begin{aligned}\psi_e^{MGB}(x,y,z;\lambda_{t,n},Q_t) &= A_e\cdot e^{-i\cdot\frac{k_t^2}{2\cdot k_H}\cdot\frac{z}{\mu}}\cdot GB(x,y,z)\cdot ce_n\left[\overline{\phi}(x,y,z);Q_t\right]\cdot\\ &\quad Je_n\left[\overline{\zeta}(x,y,z);Q_t\right]\\ \psi_o^{MGB}(x,y,z;\lambda_{t,n},Q_t) &= A_o\cdot e^{-i\cdot\frac{k_t^2}{2\cdot k_H}\cdot\frac{z}{\mu}}\cdot GB(x,y,z)\cdot se_n\left[\overline{\phi}(x,y,z);Q_t\right]\cdot\\ &\quad Jo_n\left[\overline{\zeta}(x,y,z);Q_t\right]\\ x &= f_0\cdot\mu(z)\cdot\cosh\left(\overline{\zeta}\right)\cdot\cos\left(\overline{\phi}\right)\\ y &= f_0\cdot\mu(z)\cdot\sinh\left(\overline{\zeta}\right)\cdot\sin\left(\overline{\phi}\right)\\ (x,y)\in\mathbb{R};&\left(\overline{\zeta},\overline{\phi}\right)\in\mathbb{C}\end{aligned} \tag{70}$$

with $\mu(z)$ as defined by Equation (6).

Note that for $z > 0$, the functions $\overline{\phi}(x, y, z)$ and $\overline{\zeta}(x, y, z)$ become complex such that (when performing the inverse coordinate transformation) the transverse Cartesian coordinates (x, y) remain real in the entire space (Gutiérrez-Vega & Bandres, 2005).

Like the other Wave–Gauss Beams, Mathieu–Gauss Beams diffract (cf. Figure 21). Not surprisingly, the realization of Mathieu propagation patterns was based on Mathieu Waves—Equation (33) rather than on Mathieu–Gauss Beams. The first demonstration of a low-order Mathieu Wave in the laboratory was reported by Gutiérrez-Vega et al. (2001). In a theoretical study, Chafiq, Hricha, and Belafhal (2005) propagated Mathieu Waves paraxially, by expanding Mathieu Waves in terms of Bessel Waves.

Examples of (diffracting) intensity patterns of a Mathieu–Gauss Beam (70) are shown in Figure 21. The shown starting patterns (a and b) are even and odd combinations of Mathieu Waves, respectively (cf. Figure 6C and D in Section 2.4), this time under a limiting Gaussian. The patterns in general carry a finite amount of energy. The shown patterns are propagating in a fast-expansion mode $[\omega_0 > 2/k_t]$ (cf. Section 1.6 and see Figure 2). The circular leaves-like structure in (e) and in (f) is visible under the (formed) Gaussian ring. Clearly the patterns diffract (cf. Table 3).

4. SUMMARY

In a homogenous permittivity medium (free space), Maxwell's equations are transformed to an exact HE for each of the six components of a monochromatic electromagnetic field. Using separation of variables, this three-dimensional exact HE can be reduced to a two-dimensional *transverse* equation (designated here HE—Equation 4), assuming a time-harmonic axially propagating field $\left[e^{i\cdot(k_z\cdot z-\omega\cdot t)}\right]$.

The transverse HE (Equation 4), solved in four different coordinate systems, yields four different sets of orthogonal and complete two-dimensional functions (Waves). The propagation (from $z = 0$ forward) of any input field (carrying finite energy by definition) can be accurately predicted by the sequence of decompose–propagate–recompose with any one of the four Waves as a basis. We have reviewed the basic properties of each of the associated solutions providing their mugshots, i.e., characteristic diffracting and invariant intensity patterns as well as the characteristic symmetry properties.

We note that each of the surveyed 14 Beam sets is also a basis by which paraxial propagation can be predicted. In addition, since the SVEA-PWE (Equation 5) is actually an *Optical Schrödinger Equation* of a free particle

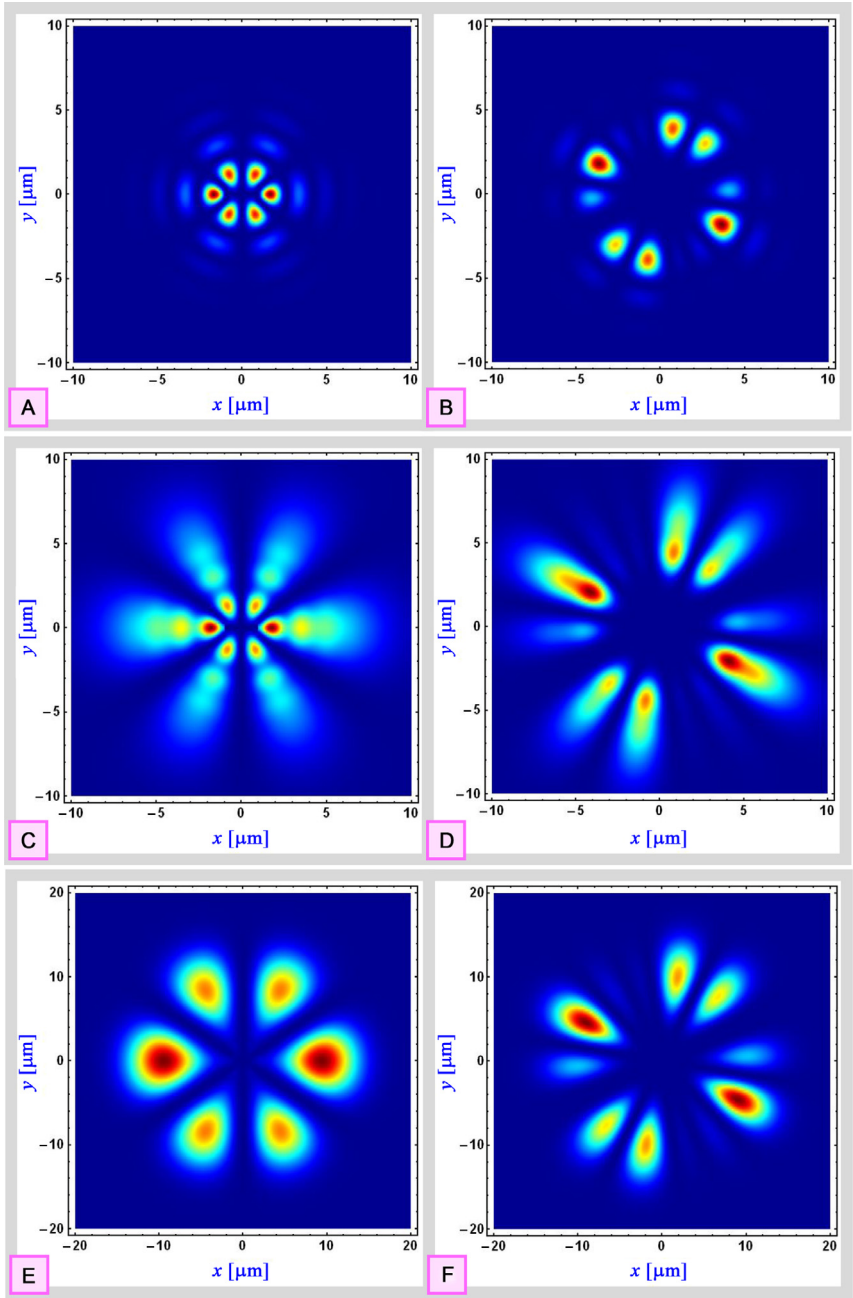

Figure 21 Intensity patterns due to Mathieu–Gauss Beams (Equations 33 and 70). Left: even. Right: combination. Top: $z = 0$. Center: $z = 30\,\mu m$. Bottom: $z = 60\,\mu m$. The shown patterns propagate in a fast-expansion mode $[\omega_0 > 2/k_t]$ (cf. Section 1.6 and see Figure 2). Clearly the patterns diffract.

(Marte & Stenholm, 1997), illuminating cross-inference can be easily exercised. Similar cross-inferences can be made for gravitational waves as well (Freise & Kenneth, 2010). Higher dimensions free-particle states were discussed by Guerrero, López-Ruiz, Aldaya, and Cossío (2011), leading to the quantum mechanical versions of the Hermite–Gauss and Laguerre–Gauss states of paraxial wave optics. Hence, the large variety of free space function sets discussed in this review are not only fundamental for classical optics but also intimately connected to quantum mechanics.

REFERENCES

Abramowitz, M., & Stegun, I. A. (1964). *Handbook of mathematical functions*. USA: Dover.

Arfken, G. B., Weber, H. J., & Harris, F. E. (2012). *Mathematical methods for physicists* (7th ed.). USA: Academic Press.

Arscott, F. M. (1967). The Whittaker–Hill equation and the wave equation in paraboloidal coordinates. *Proceedings of the Royal Society of Edinburgh, Section A*, *67*, 265.

Banders, M. A., & Gutiérrez-Vega, J. C. (2007). Airy–Gauss beams and their transformation by paraxial optical systems. *Optics Express*, *15*, 16719.

Banders, M. A., & Rodríguez-Lara, B. M. (2013). Nondiffracting accelerating waves: Weber waves and parabolic momentum. *New Journal of Physics*, *15*, 013054.

Bandres, M. A. (2008). Accelerating parabolic beams. *Optics Letters*, *33*, 1678.

Bandres, M. A. (2009). Accelerating beams. *Optics Letters*, *34*, 3791.

Bandres, M. A. (2014). *Ince Gaussian Beam*. http://www.mathworks.com/matlabcentral/fileexchange/46222-ince-gaussian-beam.

Bandres, M. A., & Gutiérrez-Vega, J. C. (2004a). Ince–Gaussian beams. *Optics Letters*, *29*, 144.

Bandres, M. A., & Gutiérrez-Vega, J. C. (2004b). Ince–Gaussian modes of the paraxial wave equation and stable resonators. *Journal of the Optical Society of America A*, *21*, 873.

Bandres, M. A., Gutiérrez-Vega, J. C., & Chávez-Cerda, S. (2004). Parabolic nondiffracting optical wave fields. *Optics Letters*, *29*, 44.

Banergee, K., Bhatnagar, S. P., Choudhry, V., & Kanwal, S. S. (1978). The anharmonic oscillator. *Proceedings of the Royal Society of London A*, *360*, 575.

Berberan-Santos, M. N., Bodunov, E. N., & Pogliani, L. (2005). Classical and quantum study of the motion of a particle in a gravitational field. *Journal of Mathematical Chemistry*, *37*, 101.

Berry, M. V., & Balazs, N. L. (1979). Nonspreading wave packets. *American Journal of Physics*, *47*, 264.

Broky, J., Siviloglou, G. A., Dogariu, A., & Christodoulides, D. N. (2008). Self-healing properties of optical Airy beams. *Optics Express*, *16*, 12880.

Carbone, L., Bogan, C., Fulda, P., Freise, A., & Willke, B. (2013). Generation of high-purity higher-order Laguerre–Gauss beams at high laser power. *Physical Review Letters*, *110*, 251101.

Chafiq, A., Hricha, Z., & Belafhal, A. (2005). Paraxial propagation of Mathieu beams through an aperture ABCD optical system. *Optics Communication*, *253*, 223.

Chu, S. C., & Otsuka, K. (2007). Numerical study for selective excitation of Ince–Gaussian modes in end-pumped solid-state lasers. *Optics Express*, *15*, 16506.

Durnin, J. (1987). Exact solutions for non-diffracting beams. I. Scalar theory. *Journal of the Optical Society of America A*, *4*, 651.

Durnin, J., Miceli, J., Jr., & Eberly, J. H. (1987). Diffraction-free beams. *Physical Review Letters*, *58*, 1499.

Dusuel, S., & Uhrig, G. S. (2004). The quartic oscillator: A non-perturbative study by continuous unitary transformations. *Journal of Physics A: Mathematical and General*, *37*, 9275.
Feynman, R. P., Leighton, R. B., & Sands, M. (1964). *The feynman lectures on physics, vol. 2*. USA: Addison-Wesley (Table 15–1).
Forbes, A. (2014). *Laser beam propagation: Generation and propagation of customized light*. USA: CRC Press.
Freise, A., & Kenneth, A. S. (2010). Interferometer techniques for gravitational-wave detection. *Living Reviews in Relativity*, *13*, 1.
Goodman, J. W. (1988). *Introduction to Fourier optics*. USA: the McGraw-Hill Companies.
Gori, F., Guattari, G., & Padovani, C. (1987). Bessel–Gauss beams. *Optics Communication*, *64*, 491.
Guerrero, J., López-Ruiz, F. F., Aldaya, V., & Cossío, F. (2011). Harmonic states for the free particle. *Journal of Physics A: Mathematical and Theoretical*, *44*, 445307.
Gutiérrez-Vega, C., Iturbe-Castillo, M. D., & Chávez-Cerda, S. (2000). Alternative formulation for invariant optical fields: Mathieu beams. *Optics Letters*, *25*, 1493.
Gutiérrez-Vega, J. C., & Bandres, M. A. (2005). Helmholtz–Gauss waves. *Journal of the Optical Society of America A*, *22*, 289.
Gutiérrez-Vega, J. C., Iturbe-Castillo, M. D., Ramírez, G. A., Tepichín, E., Rodrígez-Dagnino, R. M., Chávez-Cerda, S., et al. (2001). Experimental demonstration of optical Mathieu beams. *Optics Communication*, *195*, 35.
Gutiérrez-Vega, J. C., Rodrigez-Dagnino, R. M., Meneses-Nava, M. A., & Chavez-Cerda, S. (2003). Mathieu functions, a visual approach. *American Journal of Physics*, *71*, 233.
Hernandez-Aranda, R. I., Gutiérrez-Vega, J. C., Guizar-Sicairos, M., & Bandres, M. A. (2006). Propagation of generalized vector Helmholtz–Gauss beams through paraxial optical systems. *Optics Express*, *14*, 8974.
Hu, Y., Siviloglou, G. A., Zhang, P., Efremidis, N. K., Christodoulides, D. N., & Chen, Z. (2012). Self-accelerating Airy beams: Generation control and applications. In Z. Chen & R. Morandotti (Eds.), *Nonlinear photonics and novel optical phenomena*, USA: Springer.
Kogelnik, H., & Li, T. (1966). Laser beams and resonators. *Proceedings of the IEEE*, *54*, 1312.
Konopinski, E. J. (1978). What the electromagnetic vector potential describes. *American Journal of Physics*, *46*(5), 499.
Korotkova, O. (2013). *Random light beams: Theory and applications*. USA: CRC Press.
Levy, U., & Silberberg, Y. (2015). Free-space nonperpendicular electric–magnetic fields. *Journal of the Optical Society of America*, *32*, 647.
Marte, M. A. M., & Stenholm, S. (1997). Paraxial light and atom optics: The optical Schrödinger equation and beyond. *Physical Review A*, *56*, 2940.
Morse, P. M., & Feshbach, H. (1953). *Methods of theoretical physics. I*. USA: McGraw-Hill.
Ohtomo, T., Chu, S. C., & Otsuka, K. (2008). Generation of vortex beams form lasers with controlled Hermite– and Ince–Gaussian modes. *Optics Express*, *16*, 5082.
Porat, G., Dolev, I., Barlev, O., & Arie, A. (2011). Airy beam laser. *Optics Letters*, *36*, 4119.
Rodríguez-Lara, B. M. (2010). Normalization of optical Weber waves and Weber–Gauss beams. *Journal of the Optical Society of America*, *27*, 327.
Rodríguez-Lara, B. M. (2009). *On optical Weber waves and Weber-Gauss beams*. arXiv: 0911.2295v1.
Ruelas, A., Davis, J. A., Moreno, I., Cottrell, D. M., & Bandres, M. A. (2014). Accelerating light beams with arbitrarily transverse shapes. *Optics Express*, *22*, 3490.
Schimpf, D. N., Schulte, J., Putnam, W. P., & Kärtner, F. X. (2012). Generalizing higher-order Bessel–Gauss beams: Analytical description and demonstration. *Optics Express*, *20*, 26852.
Siegman, A. E. (1973). Hermite–Gaussian functions of complex argument as optical-beam eigenfunctions. *Journal of the Optical Society of America*, *63*(9), 1093.
Siegman, A. E. (1986). *Lasers*. USA: University Science Books.

Siviloglou, G. A., & Christodoulides, D. N. (2007). Accelerating finite energy Airy beams. *Optics Letters*, *32*, 979.
Siviloglou, G. A., Broky, J., Dogariu, A., & Christodoulides, D. N. (2007). Observation of accelerating Airy beams. *Physical Review Letters*, *99*, 213901.
Siviloglou, G. A., Broky, J., Dogariu, A., & Christodoulides, D. N. (2008). Ballistic dynamics of Airy beams. *Optics Letters*, *33*, 207.
Soifer, V. A. (2014). *Diffractive nanophotonics*. USA: CRC Press.
Stratton, J. A. (1941). *Electromagnetic theory*. USA: McGraw-Hill.
Tikhonov, A. N., & Samarskii, A. A. (2011). *Equations of mathematical physics*. Dover Publications.
Turunen, J., & Friberg, T. (2009). Propagation-invariant optical fields. *Progress in Optics*, *54*, 1–88.
Volke-Sepulveda, K., & Eugenio, L. K. (2006). General construction and connections of vector propagation invariant optical fields: TE and TM modes and polarization states. *Journal of Optics A: Pure and Applied Optics*, *8*, 867–877.
Voloch-Bloch, N., Lereah, Y., Lilach, Y., Gover, A., & Arie, A. (2013). Generation of electron Airy beams. *Nature*, *494*, 331.
Willatzen, M., & Lew Yan Voon, L. C. (2011). *Separable boundary-value problems in physics*. Germany: Wiley-VCH.
Yariv, A., & Yeh, P. (1984). *Optical waves in crystals*. USA: John Wiley& Sons.
Zhang, P., Hu, Y., Li, T., Cannan, D., Yin, X., Morandotti, R., et al. (2012). Nonparaxial Mathieu and Weber accelerating beams. *Physical Review Letters*, *109*, 193901.